

Mechanism of Delayed Storm Surge Surges in Straits: Seiche-Induced Oscillations Triggered by Typhoon Passage

Shinichiro Ozaki¹, Yoshihiko Ide², and Masaru Yamashiro²

¹Department of Civil Engineering, Graduate School of Engineering, Kyushu University, Fukuoka, Japan

²Disaster Risk Reduction Research Center, Faculty of Engineering, Kyushu University, Fukuoka, Japan

Correspondence: Shinichiro Ozaki (ozaki.shinichiro.247@s.kyushu-u.ac.jp)

Abstract. A storm surge is a phenomenon in which the sea level rises significantly due to low-pressure systems, such as typhoons, accompanied by strong winds. Once storm surge-induced flooding occurs, it can rapidly inundate low-lying areas. Generally, the primary contributor to storm surge is wind set-up, where wind blows directly toward the coastline. As such, it is well-known that severe storm surges occur at typhoon's closest approach because strong winds blow directly to the coastline. However, when during Typhoon Maysak (2020) struck, delayed flooding was observed along the northern coast of Kyushu Island (NCKI), which located in the south of the Tsushima Strait, the sea level rose and flooding occurred approximately half a day approximately 10 hours after the typhoon had passed. At NCKI, strong winds did not blow perpendicular to the coastline during the typhoon, and at the time of the flooding By that time, both atmospheric pressure and wind had already weakened. Thus, the storm surge could not be explained by wind set-up or intensity had substantially weakened, indicating that conventional mechanisms—such as wind setup and the inverted barometer effect. We examined storm surge observations for typhoons that impacted NCKI over the past 20 years and revealed a tendency for two peaks in storm surge when typhoons passed—could not fully account for the phenomenon. This study explores the mechanisms behind delayed storm surges along the NCKI through a combination of observational data analysis, storm surge simulations, and continuous wavelet transform (CWT) analysis. The results reveal that typhoons passing through the western channel of the strait. The second peak was identified as the maximum storm surge height, occurring approximately Tsushima Strait (WCTS-type) frequently generate double-peaked storm surge anomaly, with the second peak being both larger and longer-lasting than the first. Spectral analysis identified dominant oscillations with periods of approximately 5 and 10 hours after the typhoon had passed. The first peak occurred when the typhoon was closest to NCKI, coinciding with the time of minimum atmospheric pressure. This was attributed to the sea level rise caused by the inverted barometer effect. After the first peak, oscillations with a period of approximately 10 hours were observed, resulting in the second peak. NCKI, located along, corresponding to the natural modes of the Tsushima Strait. These oscillations, interpreted as (1, is subject to the geographical characteristics of the strait 1) and (1, which likely caused the oscillations leading to 0) mode seiches, are excited by the release of potential energy trapped within the strait once the external forcing has subsided. Notably, the maximum storm surge. To identify the oscillations that occurred after the 5-hour mode appears to be strongly influenced by the Coriolis effect. Our findings reveal a previously unrecognized storm surge mechanism in which significant surges occur not during, but after, a typhoon's passage, a continuous wavelet transform was applied to the results of storm surge simulations for time-frequency analysis. As a result, it was found that two types of seiches in a two-dimensional spatial domain of the strait (5-hour and 10-hour periods) occurred after the typhoon's passage. These seiches were triggered by the release of potential energy as external forces weakened following the typhoon's transit through the strait. Furthermore, the seiches were observed to occur approximately two hours earlier when the external force was wind, compared to when it was atmospheric

pressure. This is because the time variation of atmospheric pressure drop is slower than that of wind direction. In this study, we identified the occurrence of anomalous storm surges caused by typhoons passing through a strait under specific conditions and conducted a detailed investigation of their generation mechanisms, and demonstrate storm surges can occur even after a typhoon has passed and improve understanding of storm surge characteristics in straits through a strait. This delayed response arises from resonant amplification caused by modal oscillations within the strait, particularly in cases where typhoon tracks curve westward. The study underscores the critical roles of strait geometry, natural oscillation modes, and the timing of external forcing in shaping storm surge behavior. These insights extend beyond the NCKI and are relevant to other semi-enclosed strait regions worldwide that exhibit similar meteorological and geographical characteristics, even though the extent of influence from oscillation modes, periods, and amplitudes may vary depending on the strait's horizontal scale, water depth, and latitude.

Copyright statement. © 2025 Ozaki et al. This work is distributed under the Creative Commons Attribution 4.0 License. To view a copy of this license, visit <https://creativecommons.org/licenses/by/4.0/>.

1 Introduction

Storm surges are phenomena where events in which sea levels rise significantly due to low air atmospheric pressure and strong winds, such as during a typhoon. Once typically associated with typhoons. When a storm surge occurs, extensive flooding rapidly affects it can rapidly inundate low-lying coastal areas, causing widespread flooding. Climate projections that account for global warming suggest incorporate the effects of global warming indicate that storm surge heights will increase worldwide in the future (Balaguru et al. (2016), Yang et al. (2020), and Mori et al. (2022)) are likely to increase globally (Balaguru et al. (2016); Yang et al. (2020); Mori et al. (2022)). To mitigate reduce the damage caused by storm surges, it is crucial vital to implement both structural measures, such as storm surge barriers (Miguel Esteban (2014)), and non-structural measures. A thorough understanding of the nature of storm surges is essential for devising effective , such as real-time forecasting systems (Igarashi and and (2021)). A comprehensive understanding of storm surge dynamics is therefore crucial for developing effective protection strategies.

Several widely accepted theories explain the mechanisms explain the generation of storm surges. One such theory is the The inverted barometer effect , where sea levels rise as if drawn up by low air pressure . Other theories include wind set-up and wave set-up (Wunsch and Stammer (1997), Walton and Dean (2009), and Wu et al. (2018)). Wind set-up occurs when strong winds blow perpendicular to the shoreline, driving seawater ashore and raising sea levels. Wave set-up is caused by accounts for sea-level rise caused by low atmospheric pressure (e.g., Wunsch and Stammer (1997)), while wind setup refers to the rise in sea level due to strong winds forcing seawater shoreward (e.g., Walton and Dean (2009)). This occurs when coastal winds drive surface water toward the shore, causing accumulation in shallow regions and elevating the local sea level. Wave setup, in contrast, results from wave breaking and radiation stress (e.g., Wu et al. (2018)). These mechanisms are most active when typhoons are nearest typically most pronounced when a typhoon is closest to the target area due to the strongest winds and lowest air pressure . Additionally, previous studies have identified other , as wind speeds and pressure gradients peak during this time. Additional causes of storm surges , such as seiche in bays and on continental shelves, Ekman set-up where seawater is pushed to the shore by the Coriolis

force from prolonged winds include Ekman setup, wherein sustained winds blowing parallel to the shore coast induce shoreward water transport via the Coriolis effect (e.g., Kim et al. (2010), Shen and Gong (2009)), and the propagation of high water levels due to land shelf waves (Kim et al. (2010), Shen and Gong (2009)), and shelf waves, which carry elevated water levels along the coast after the storm (e.g., Kennedy et al. (2011)). Among these theories, wind set-up is the most significant contribution to the surge. Among these mechanisms, wind setup is generally recognized as the primary contributor to storm surge height. Wind set-up height is directly proportional to the wind fetch and inversely proportional to water depth. Regions that have historically suffered significant storm surge damage are often bays facing the ocean, characterized by geographical conditions that amplify wind set-up (Bilskie et al. (2016), Bhaskaran et al. (2020), Nakajo et al. (2015), Ide et al. (2020)).

Conversely, most vulnerable to major storm surges often include ocean-facing bays with geographical features that amplify wind-driven water accumulation (Bilskie et al. (2016); Bhaskaran et al. (2020); Nakajo et al. (2015); Ide et al. (2020)). Significantly, even in straits with relatively short fetch, significant lengths, substantial storm surges can happen where winds blow directly. For example, still occur due to wind setup. For instance, in East Asia, Tsushima Strait, located between Kyushu Island and the Korean Peninsula (see the Tsushima Strait is a significant waterway located within the Northwest Pacific region (Figure 1), is frequently hit a). This strait is frequently impacted by typhoons. Typhoons approaching the Tsushima Strait often move northeastward. These typhoons often track northeast through the strait, after which they tend to either make landfall on the southern coast of the Korean Peninsula (SCKP,) (Figure 1) or enter b) or continuing into the Sea of Japan. Sanba (2012), the most powerful Typhoon Sanba—the strongest typhoon of 2012, moved—passed through the Tsushima Strait, affecting coastal areas on the SCKP where wind blow directly to the coastal line. The typhoon was accompanied by strong winds with a bringing maximum instantaneous wind speed of over speeds exceeding 20 m/s, and storm surge heights over 100 cm added surge height (at Gwangyang (Figure 1b), near the center of the SCKP region (Yoon et al. (2014)). Typically, when a typhoon traverses the western channel of the Tsushima Strait (WCTS), a significant storm surge is observed along the SCKP, primarily driven by wind setup. As illustrated in Figure 2a, when the typhoon is centered over the strait, the counterclockwise wind circulation characteristic of Northern Hemisphere typhoons generates strong onshore winds directed toward the SCKP. This results in substantial wind-driven water accumulation. Additionally, the surge is further enhanced by the inverted barometer effect, which raises sea level under conditions of low atmospheric pressure.

In contrast, on the northern coast of Kyushu Island (NCKI, see) (Figure 1), located b), which lies across the Tsushima Strait from SCKP, large storm surges generally unlikely occur during typhoons approaching because a strong wind does not blow directly to the coastal line. The SCKP, significant storm surges are generally considered unlikely during typhoon approaches. When a typhoon is located over the Tsushima Strait, southwesterly winds typically prevail over the NCKI (Figure 2a). Because the winds drive seawater away from the coast, the local sea level tends to drop—opposite to the rise observed along the SCKP. However, when during Typhoon Maysak (2020) struck NCKI, extensive areas were inundated, leading to house flooding and, widespread inundation occurred along the NCKI, causing flooding and major traffic disruptions (Niimi et al. (2022)). Although Typhoon Maysak passed through the western channel of the Tsushima Strait (WCTS, see Figure 1) and WCTS, it did not make landfall at NCKI. Remarkably, the inundation on the NCKI (see Figure 3). Notably, flooding occurred approximately 10 h after the closest approach to NCKI, with the typhoon still over hours after the typhoon's closest approach—by which time the typhoon had already moved more than 600 km away from NCKI. The storm surge. Typically,

once a typhoon enters the Sea of Japan after passing through the Tsushima Strait, its influence on the NCKI diminishes: strong winds subside (Figure 2b), and atmospheric pressure returns to near-normal sea level conditions. Therefore, the storm surge observed in this event cannot be attributed to the inverted barometer effect, wind set-up, or wave set-up, because atmospheric typical storm surge mechanisms such as wind setup, wave setup, or the inverted barometer effect, as the local pressure had risen to about 1000 hPa, and there were around 1,000 hPa and no strong winds were present at the time of flooding.

In research focused on storm surges in NCKI, Hong and Yoon (1992) investigated the storm surge mechanism for Holly (1984). They compared the observed storm surge at NCKI and SCKP, and reported that there is a time lag of approximately half a day between the maximum peak of storm surge anomalies between NCKI and SCKP. Niimi et al. (2022) studied the effect of Coriolis force to the storm surge at NCKI during Maysak (2020) and concluded that oscillations occur in the Tsushima Strait after the passage of the typhoon regardless of the presence of the Coriolis force inundation. Previous studies have suggested that delayed storm surges along the NCKI may be linked to oscillatory responses within the Tsushima Strait (e.g., Hong and Yoon (1992); Niimi et al. (2022)). While storm surge dynamics have been studied in other straits, such as the Taiwan Strait Zhang et al. (2010), the Strait of Georgia Soontiens et al. (2016), and the maximum surge height becomes larger when the Coriolis force is present. As indicated by these previous studies, oscillations occur in Singapore Strait Tkalich et al. (2013), these investigations do not report delayed surge responses following typhoon passage. In contrast, the Tsushima Strait following the passage of a typhoon, and it is highly likely that these oscillations lead to storm surges with a delay of approximately half a day. Storm surge mechanisms in other straits include the following Zhang et al. (2010), Soontiens et al. (2016) and Tkalich et al. (2013). In such straits, there is also a possibility that storm surges may occur at unexpected times after the passage of a typhoon. Therefore, this study appears to exhibit a unique behavior: storm surges can occur several hours after a typhoon has passed, likely due to natural oscillations within the strait.

Although storm surges along the NCKI have been documented in previous studies, the delayed occurrence of these surges following typhoon passage through the WCTS remains insufficiently understood. This study offers new insights into the phenomenon by highlighting the role of coastal topography in generating delayed surge responses. To investigate this, we analyzed multiple typhoon events from the past two decades, aiming to elucidate the mechanism behind surge increases that occur after typhoon passage, with mechanisms underlying post-passage surge increases, using the Tsushima Strait as a representative case, using observational data and numerical simulations. Our analysis integrates observational records, numerical storm surge simulations, and spectral analysis via wavelet transforms. Through this approach, we identified dominant oscillation modes with periods of approximately 10 and 5 hours that were consistently present during delayed storm surge events.

The structure of this paper is as follows: In Section ??, we outline the methods for analyzing observational data and provide details of the numerical simulations. Section ?? explores the mechanisms of storm surge generation specific to NCKI. organized as follows. Section 2.1 describes the geographical and oceanographic characteristics of the Tsushima Strait. Section 3 introduces the selected typhoons analyzed in this study. Section 4 presents the analysis of observed storm surges and meteorological data. Section 5 outlines the numerical simulations conducted to reproduce the storm surge behavior. Section 6 explains the application of continuous wavelet transform (CWT) for spectral analysis of the simulated results. Section 7 discusses the physical mechanisms behind the observed phenomena. Finally, Section 8 summarizes the findings main findings and implications of this study.

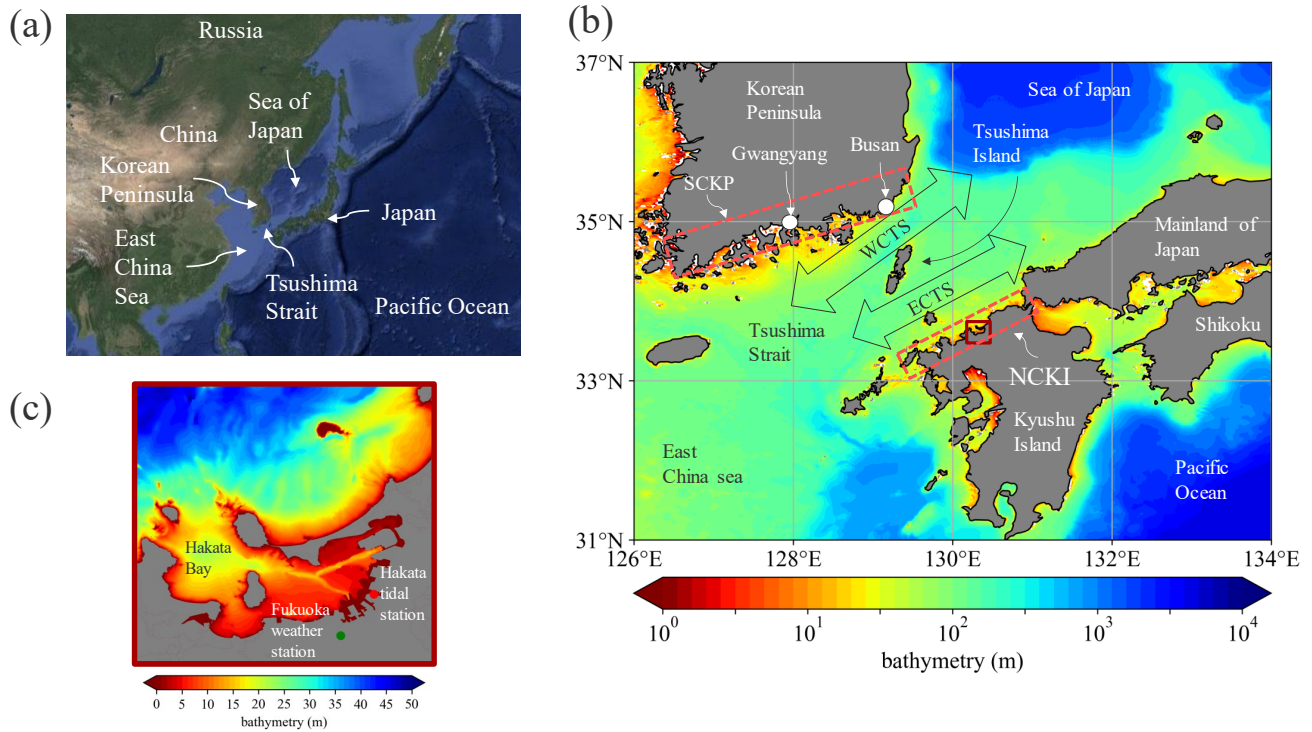


Figure 1. Bathymetry of Bathymetric maps illustrating the Tsushima Strait, with geographical context and study regions. (a) Regional map displaying the points Northwest Pacific. (b) Magnified view showing the detailed bathymetry of the tidal stations around the Tsushima Strait, and the right side of the figure shows an enlarged . (c) Close-up view of presenting the bathymetry within Hakata Bay, with the points of the tidal station and the weather station.

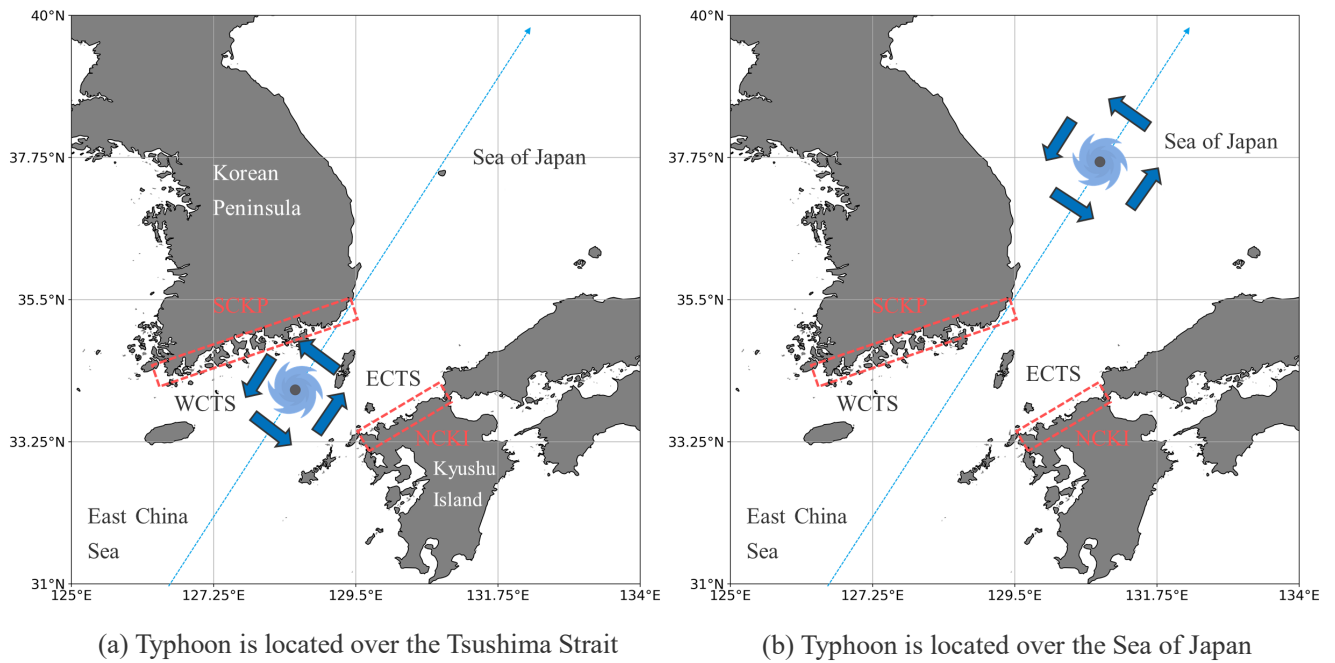


Figure 2. Schematic figure of typhoon positions and wind directions during its passage through the WCTS: (a) when the typhoon is located over the Tsushima Strait; (b) when the typhoon is located over the Sea of Japan.

2 Data and Methodology Study Area

2.1 Typhoons

We selected the typhoons used in this study as follows: The Tsushima Strait, located in the Northwest Pacific region as shown in Figure 1a, is situated in East Asia between the Korean Peninsula to the northwest and Kyushu Island in Japan to the southeast (Figure 1b). This strait is a typical typhoon-prone region, particularly during the summer months, and frequently experiences strong winds and storm surges associated with typhoon passages. The average water depth of the strait is approximately 80 m. The strait connects two major bodies of water: the Sea of Japan to the north and the East China Sea to the south. The Sea of Japan is characterized by deep waters, while the East China Sea is comparatively shallow. This stark depth contrast contributes to the complex oceanographic dynamics within the strait. Tsushima Island is located in the center of the strait (Figure 1b), dividing it into two distinct channels: the WCTS, located between Tsushima Island and the SCKP, and the ECTS, located between Tsushima Island and the NCKI. Of the two, the WCTS is slightly deeper and plays a more significant role in water exchange and current dynamics across the strait.

Hakata Bay, located in the central part of the NCKI, is shown in the Figure 1c. The surrounding area includes Fukuoka City, one of the most densely populated urban centers in the region. The bay extends approximately 20 km east–west and 10 km north–south, forming a semi-enclosed coastal basin. The Hakata tidal station, situated on the eastern side of the bay, has provided continuous sea-level records since 1998. Additionally, the Fukuoka weather station, located on the southern side of the bay, continuously monitors atmospheric pressure, wind speed, and wind direction.

3 Selected Typhoons

We selected various typhoons for analysis through the following process. The tracks of the selected typhoons are shown in Figure 3. First, we obtained data on best track data for 1,898 typhoon tracks from the best track data provided typhoons recorded from 1951 to 2022 by the Japan Meteorological Agency (JMA; <https://www.jma.go.jp/jma/jma-eng/jma-center/rsmc-hp-pub-eg/besttrack.html>). Second, The full set of typhoon tracks is shown in Figure 3a. Next, we identified 599 typhoons from that occurred between 1998 to and 2022 for which tide level observation, during which tide-level data were available for at the Hakata tidal station. Finally, from these 599 typhoons, we (Figure 3b). From this subset, we then selected 67 that typhoons whose tracks passed within a 300 km radius of the Hakata tidal station.

3.1 Storm surge anomalies

We calculated the storm surges caused by for detailed analysis (Figure 3c). To calculate storm surge anomalies associated with the 67 selected typhoons as follows: First, we obtained tidal level, we used the following method. First, sea-surface elevation data sampled at 30-s intervals from 30-second intervals from 1998 to 2022 were obtained from the Hakata tidal station for the period 1998 to 2022 via the RDMDDB Data Retrieval System (via the Regional Delayed Mode Data Base (RDMDDB, <https://near-goos1.jodc.go.jp/vpage/search.html>)). Second, we performed a harmonic analysis on the obtained tidal data to derive harmonic constituents (observed data using the pytides

0.0.4 package (<https://github.com/sam-cox/pytides>) to extract tidal constituents, including Z0, M2, S2, N2, K1, M4, O1, M6, MK3, S4, MN4, nu2, S6, mu2, 2N2, OO1, lambda2, S1, M1, J1, Mm, Ssa, Sa, MSF, Mf, rho1, Q1, T2, R2, 2Q1, P1, 2SM2, M3, L2, 2MK3, K2, M8, MS4) using pytides 0.0.4 () and others—a total of 39 components. Third, we calculated storm surge anomalies were calculated by subtracting the astronomical tides reconstructed astronomical tide from the observed tidal data. To account for annual variations, we averaged the anomalies sea-surface elevation. To remove interannual variability, we computed the average anomaly at the time of each typhoon 's approach typhoon approach for each year and subtracted this average mean value. Finally, we selected identified 16 typhoons with maximum that produced maximum storm surge anomalies of 30 cm or more greater at the Hakata tidal station . (Figure 3d).

3.1 Wind and air pressure

We obtained wind speed, wind direction, and air pressure at the sea surface for the period 1998 to The selected typhoons can be categorized into two types based on their tracks around the Tsushima Strait: WCTS-type and ECTS-type typhoons. WCTS-type typhoons follow a path from the SCKP through the WCTS, approaching the Hakata area from the northwest. This category includes Typhoons Rusa (2002), Maemi (2003), Megi (2004), Sanba (2012), Chaba (2016), Kong-rey (2018), Maysak (2020), Haishen (2020), and Hinnamnor (2022 from the). ECTS-type typhoons, on the other hand, move from the ECTS toward the NCKI, generally approaching from the northeast. This group includes Typhoons Bart (1999), Chaba (2004), Songda (2004), Shanshan (2006), Danas (2013), Goni (2015), and Tapah (2019). These two classifications are used throughout the following analysis.

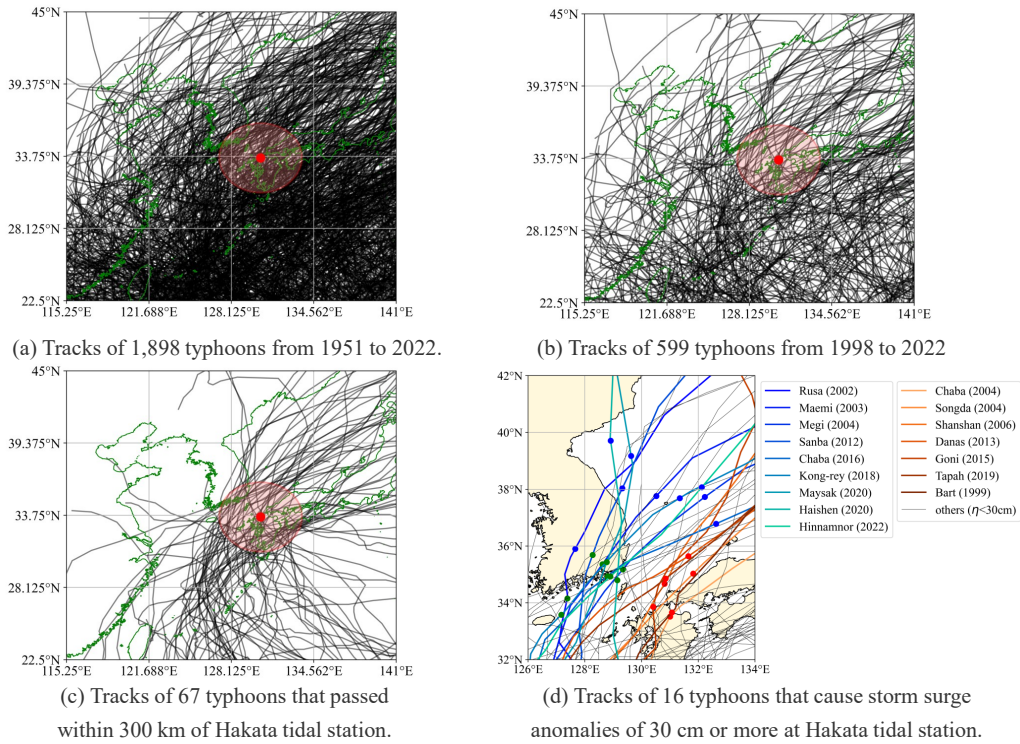


Figure 3. Tracks of selected typhoons in this study. (a) Tracks of 1,898 typhoons recorded by JMA from 1951 to 2022. (b) Tracks of 599 typhoons that occurred between 1998 and 2022, during which tide-level observations were available at the Hakata tidal station. (c) Tracks of 67 typhoons that passed within a 300 km radius of the Hakata tidal station. (d) Tracks of 16 typhoons that caused storm surge anomalies of 30 cm or more at the Hakata tidal station between 1999 and 2022. In panels (a)–(c), black curves represent typhoon tracks, the red dot indicates the location of the Hakata tidal station, and the red circle marks the 300 km radius around the station. In panel (d), red and blue lines show the tracks of the 16 typhoons that generated significant storm surge anomalies. Red lines correspond to ECTS-type typhoons, while blue lines correspond to WCTS-type typhoons. The remaining typhoons are shown in black lines. For WCTS-type typhoons, green dots indicate the timing of the first surge peak at the Hakata tidal station, and blue dots indicate the second peak. For ECTS-type typhoons, red dots indicate the timing of the maximum storm surge anomaly (as referenced by arrows in Figure 4).

4 Observed Storm Surge and weather data Characteristics

We examined the observed data, such as storm surge anomalies, wind, and atmospheric pressure, and categorized them according to the typhoon tracks. The black lines in Figure 4 shows the time series of storm surge anomalies acquired at the Hakata tidal station for both WCTS and ECTS-type typhoons.

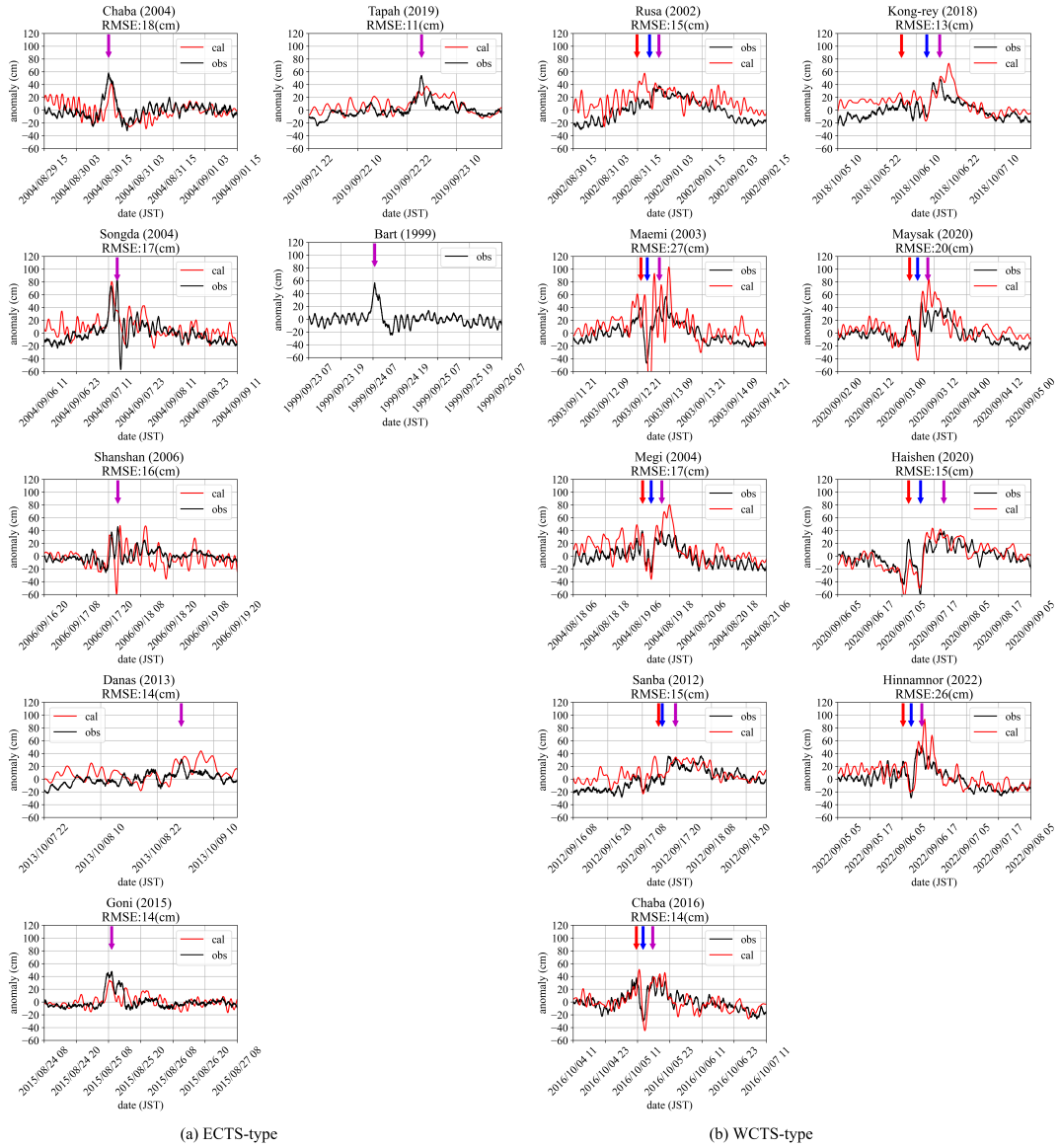
storm surge anomalies during ECTS-type typhoons tend to rise sharply over a short period (indicated by purple arrows in Figure

fig:Hakata_zetaa). Typhoons Chaba (2004) and Bart (1999) exhibit a single peak in the storm surge anomaly, while Songda (2004), Shanshan (2004), and Goni (2015) exhibit a two-peaked pattern.

The positions of the ECTS-type typhoons at the times indicated by the purple arrows in Figure 4a are marked with red dots along their tracks in Figure 3d. The peak storm surge anomaly is observed just after the typhoon passes over Hakata Bay. As a representative ECTS typhoon, Figure 5a shows the time series of the wind and air pressure at the Fukuoka weather station (see Figure 1) which is the nearest station to the Hakata tidal station during Goni (2015). At 08:00 on August 25, provided by JMA (2015), when the storm surge anomaly reaches its maximum, the air pressure also drops to its minimum value of 970 hPa, and a northerly wind is observed (purple arrows in Figure 5a). These observations indicate that the rapid rise in storm surge anomalies during ECTS-type typhoons can be attributed to a combination of the inverted barometer effect and wind setup. As these typhoons pass close to Hakata Bay, the sharp drop in atmospheric pressure causes a corresponding rise in sea level via the inverted barometer effect. Additionally, once the typhoon moves slightly beyond the bay, northerly onshore winds develop, inducing wind setup that further elevates the sea level.

4.1 Numerical simulation

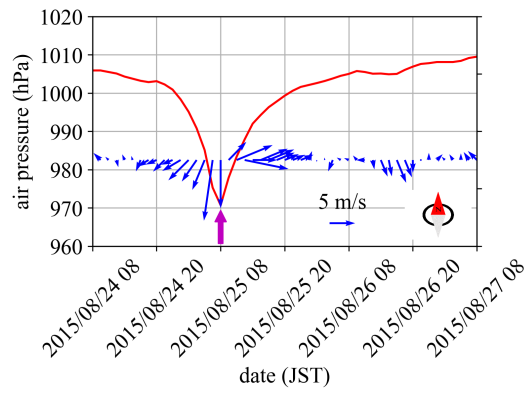
In contrast, storm surge anomalies associated with WCTS-type typhoons exhibit unusual temporal patterns. Typically, the surge anomaly increases as the typhoon approaches Hakata Bay, reaching an initial peak (green dot in Figure 3; red arrow in Figures 4b). This is followed by a rapid decrease (blue arrow in Figures 4b), and then a second increase resulting in another peak (purple arrow in Figures 4b). The location of the typhoon at the time of the second peak is indicated by a blue dot in Figure 3, showing that the typhoon had already entered the Sea of Japan. Typhoon Sanba (2012) is a notable exception, as it did not exhibit this two-peaked pattern at the Hakata tidal station. Figure 5b presents the time series of wind and atmospheric pressure at the Fukuoka weather station during Typhoon Hinnamnor (2022). The first storm surge anomaly peak coincides with the typhoon's closest approach to the NCKI, when the minimum pressure of 991.4 hPa is recorded—consistent with the inverted barometer effect (red arrows in Figures 4b and 5b). However, the second peak occurs after the typhoon has moved into the Sea of Japan, at which time local pressure at the NCKI rises to around 1,000 hPa, and wind speeds drop below 5 m/s (purple arrows in Figures 4b and 5b). Thus, this second surge peak cannot be explained by the inverted barometer effect or wind setup alone. Accordingly, this study aims to clarify the physical mechanisms responsible for the second surge peak observed during WCTS-type typhoons.



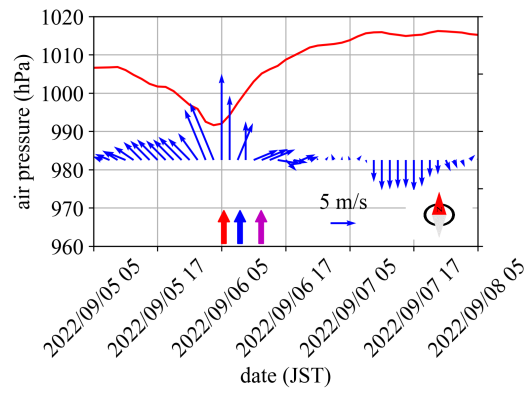
(a) ECTS-type

(b) WCTS-type

Figure 4. Time series of storm surge anomalies at the Hakata tidal station for (a) ECTS-type and (b) WCTS-type typhoons. The black curve represents the observed storm surge anomaly, while the red curve shows the simulated anomaly. Red, blue, and purple arrows indicate the timing of the first peak, local minimum, and second peak (or maximum), respectively.



(a) Goni (2015): ECTS-type



(b) Hinnamnor (2022): WCTS-type

Figure 5. Time series of air pressure and winds at Fukuoka weather station for (a) ECTS (Goni, 2015) and (b) WCTS (Hinnamnor, 2022) typhoons.

5 Numerical Simulation

5.1 Model Setup

205 An unstructured grid Finite-Volume Community Ocean Model (FVCOM, Chen et al. (2003)) was used to calculate the storm surge storm surges associated with the input meteorological data for air pressure and winds. FVCOM utilizes wind. The FVCOM employs the finite-volume method and employs , using a triangular grid system in the horizontal plane and generalized terrain-following coordinates in the vertical direction (Yoon and Shim (2013)). The model incorporates the modified level 2.5 Mellor and Yamada (1982) and Smagorinsky (1963)(Mellor and Yamada (1982), Smagorinsky (1963)) turbulent closure schemes for vertical and horizontal mixing. The Its governing equations include the following equations of motion and the continuity equation Continuity equations:

$$\frac{\partial u}{\partial t} + u \frac{\partial u}{\partial x} + v \frac{\partial u}{\partial y} + w \frac{\partial u}{\partial z} - f v = -\frac{1}{\rho_0} \frac{\partial(p_H + p_a)}{\partial x} + \frac{\partial}{\partial z} \left(K_m \frac{\partial u}{\partial z} \right) + F_u, \quad (1)$$

$$\frac{\partial v}{\partial t} + u \frac{\partial v}{\partial x} + v \frac{\partial v}{\partial y} + w \frac{\partial v}{\partial z} + f u = -\frac{1}{\rho_0} \frac{\partial(p_H + p_a)}{\partial y} + \frac{\partial}{\partial z} \left(K_m \frac{\partial v}{\partial z} \right) + F_v, \quad (2)$$

$$\frac{\partial w}{\partial t} + u \frac{\partial w}{\partial x} + v \frac{\partial w}{\partial y} + w \frac{\partial w}{\partial z} = \frac{\partial}{\partial z} \left(K_m \frac{\partial w}{\partial z} \right) + F_w, \quad (3)$$

$$215 \quad \frac{\partial u}{\partial x} + \frac{\partial v}{\partial y} + \frac{\partial w}{\partial z} = 0, \quad (4)$$

where x , y , and z are horizontal and vertical positions; , u , v , and w are the velocities in the x , y , and z directions, respectively; , t is time; represents time, p_a is air pressure at the air pressure on the sea surface; , p_H is hydrostatic pressure; the hydrostatic pressure, f is the Coriolis parameter; , g is the acceleration due to gravity; , K_m is the vertical eddy viscosity; , and F_u , F_v , and F_w are the horizontal and vertical momentum diffusion terms, respectively. The FVCOM utilizes the finite-volume method for discretization and can be applied using either Cartesian (xy) or geographic (latitude and longitude) coordinates. A detailed description of the discretization procedures is available in (Chen et al. (2003)).

The boundary conditions at on the sea surface are as follows: defined as

$$K_m \left(\frac{\partial u}{\partial z}, \frac{\partial v}{\partial z} \right) = \frac{1}{\rho_0} (\tau_{sx}, \tau_{sy}), \quad (5)$$

$$w = \frac{\partial \eta}{\partial t} + u \frac{\partial \eta}{\partial x} + v \frac{\partial \eta}{\partial y} \quad (6)$$

225 where η is the height of the free surface. , ρ_0 is a the density of seawater. , and τ_{sx} and τ_{sy} are the x - and y -axis components of the sea surface shear stress and are expressed using the following equations, respectively:

$$(\tau_{sx}, \tau_{sy}) = \rho_a C_s U (U_{10}, V_{10}), \quad (7)$$

$$U = \sqrt{U_{10}^2 + V_{10}^2} \quad (8)$$

where with U_{10} and V_{10} are being the x - and y -axis components of the wind speed at 10 m above the sea surface, respectively, 230 ρ_a is a being the density of the atmosphere, and C_s is being the wind drag coefficient, which was calculated by Large and Pond (1981)'s

formula is calculated as follows (Large and Pond (1981)):

$$C_s = \begin{cases} 1.20 \times 10^{-3} & \text{if } 0 \leq U < 11\text{m/s} \\ (0.49 + 0.065U) \times 10^{-3} & \text{if } 11\text{m/s} \leq U \end{cases} \quad (9)$$

We adopted this formulation to be consistent with the wind stress setting used in Niimi et al. (2022), which provided a validated reference framework for storm surge simulations in this region.

235 The boundary conditions at on the seafloor are as follows: defined as

$$K_m \left(\frac{\partial u}{\partial z}, \frac{\partial v}{\partial z} \right) = \frac{1}{\rho_0} (\tau_{bx}, \tau_{by}), \quad (10)$$

$$w = -u \frac{\partial h}{\partial x} - v \frac{\partial h}{\partial y} \quad (11)$$

where h is the water depth., and τ_{bx} and τ_{by} are the x - and y -axis components of the seafloor shear stress and are expressed as follows, respectively:

$$240 (\tau_{bx}, \tau_{by}) = \rho_0 C_b \sqrt{u^2 + v^2} (u, v). \quad (12)$$

The bottom drag coefficient was is determined by matching a logarithmic bottom layer to the model at a height z_a above the bottom. from the bottom:

$$C_b = \max \left(\kappa^2 / \ln \left(\frac{z_a}{z_0} \right)^2, 0.0025 \right) \quad (13)$$

where $k = 0.4$ is the von Karman constant, Kármán constant and z_0 is the bottom roughness parameter, which is basically
245 0.001 m in ocean. the ocean.

The model domain is shown depicted in Figure 6. It This domain spans an extensive area from 125° to 135° E in longitude and from 27° to 36° N in latitude (Figure 6a). Coastal lines are For the FVCOM input, we provided x - y coordinates corresponding to the longitude and latitude, respectively. Coastal lines were sourced from the Ministry of Land, Infrastructure, Transport and Tourism in , and Tourism of Japan (<https://nftp.mlit.go.jp/ksj/gml/datalist/KsjTmplt-C23.html>).
250 ter depth data are were obtained from the Japan Hydrographic Association (<https://www.jha.or.jp/jp/shop/products/btdd/>) and the Japan Oceanographic Data Center (https://www.jodc.go.jp/jodcweb/JDOSS/infoJEGG_j.html) and are interpolated to , and they were interpolated into the mesh using an inverse distance weighting method. A large unstructured grid with a resolution of 50 km was used for the open sea, while whereas very small triangular meshes with a resolution of 300 m were employed along Kyushu Island , including and Hakata Bay. Figure 6b is the enlarged image of the area surrounded by the red
255 box in Figure 6a, which is an unstructured grid around Hakata Bay. The model uses The model used three sigma levels in the vertical direction. The triangular grid consists of comprised 254,335 nodes and 483,582 elements. Winds at a height of 10 m above the sea surface and air pressure at the sea surface are obtained from MSM (were obtained from Meso-Scale Model (MSM, https://www.data.jma.go.jp/suishin/cgi-bin/catalogue/make_product_page.cgi?id=MesModel), which provides provided grid point values from an hourly weather forecast for Japan and its surrounding ocean area , calculated at a finer grid spacing

260 (5 km) than the global model. In addition, we conducted three simulation cases: (1) both atmospheric pressure and wind forcing, (2) pressure-only forcing, and (3) wind-only forcing. For each typhoon, the computation period is 8 days with a time step of 1.0 s. The initial water level is set at mean sea level, and tides and wind waves are not considered. For typhoon Bart (1999), no calculated values are available due to the absence of MSM.

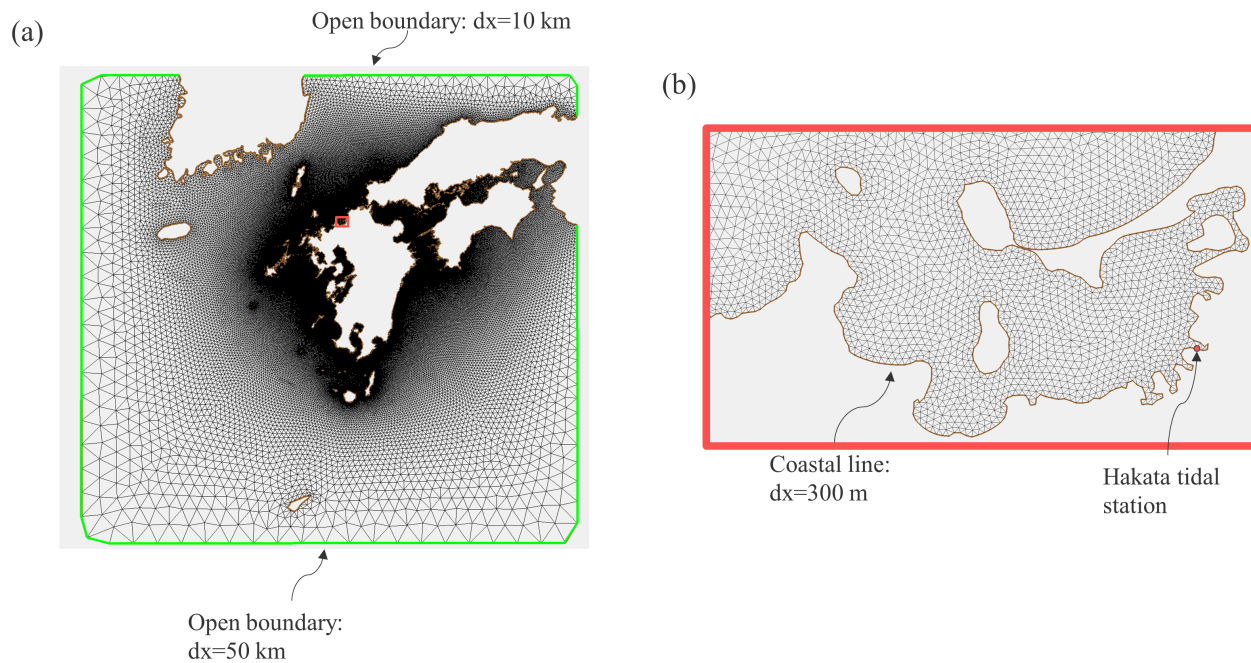


Figure 6. Overview of the model domain: (a) grid composition ; and (b) enlarged grid view of Hakata Bay).

5.2 Wavelet transform Validation

265 We conducted spectral analysis using continuous wavelet transform (CWT) to investigate the oscillatory components within the storm surges. CWT is a method suitable for non-stationary spectral analysis. In CWT, a small wave known as the mother wavelet is utilized. Frequency analysis is performed by comparing the mother wavelet with the wave of interest. The mother wavelet is given by:

$$\psi_{a,b}(t) = \frac{1}{\sqrt{a}} \psi\left(\frac{t-b}{a}\right)$$

270 where, $\psi(t)$ is the mother wavelet, t is time, a is a scale and b is shift. When a increases, the mother wavelet is stretched, making it more suitable for analyzing longer waves. Increasing b results in a parallel shift in the positive direction along the time axis. For the mother wavelet defined by scale a and shift b , denoted by $\psi_{a,b}(t)$, the continuous wavelet transform is expressed as follows:

$$W_{\psi_{a,b}}[x(t)] = \int_{-\infty}^{\infty} x(t) \psi_{a,b}^*(t) dt$$

where $x(t)$ is the signal of interest and $*$ denotes the complex conjugate. By continuously varying the scale a and shift b , the continuous wavelet transform maps to a two-dimensional plane of (a, b) , allowing for frequency analysis in the time domain. In this study, the following complex Morlet wavelet is utilized as the mother wavelet:

275
$$\psi(t) = \frac{1}{\sqrt{\pi B}} \exp\left(-\frac{t^2}{B}\right) \exp(2\pi C j t)$$

where j is the imaginary unit, $B = 1.5$, and $C = 1.0$. In CWT, we used PyWavelets (Lee et al. (2019)).

6 Result and discussion

5.1 Time series analysis

280 Figure 3 illustrates the tracks of 67 typhoons that passed within a 300 km radius of the Hakata tidal station from 1999 to 2022. The red and blue lines represent the 16 typhoon paths that caused storm surge anomalies of 30 cm or more in Hakata Bay, while the black lines show the paths of the remaining typhoons. The typhoon paths can be categorized into two patterns. The first, WCTS-type typhoons, denoted by the red lines in Figure 3, follow a route from the SCKP to WCTS. This category includes typhoons such as Rusa (2002), Maemi (2003), Megi (2004), Sanba (2012), Chaba (2016), Kong-rey (2018), Maysak (2020), Haishen (2020), and Hinnamnor (2022). The second, ECTS-type typhoons, indicated by the blue lines in Figure 3, travel from the ECTS to the NCKI, including Bart (1999), Chaba (2004), Songda (2004), Shanshan (2006), Danas (2013), Goni (2015), and Tapah (2019).

285 Figure 4 displays Red lines in Figure 4 show the time series of storm surge anomalies at the Hakata tidal station for both WCTS-type and ECTS-type typhoons. The black lines represent the observed values, while the red lines indicate the values calculated WCTS and ECTS typhoons, as simulated by FVCOM. For Bart (1999), no calculated values are available due to the absence of meteorological data (MSM). For both WCTS-type and ECTS-type typhoons, the calculated values exhibit a pronounced 2-h periodic seiche at Hakata Bay (Yamashiro et al. (2016)), but Below each panel title, the root mean square error (RMSE) between the observed and simulated surge anomalies is indicated as a quantitative measure of model accuracy. Overall, the general trend of the observed time series is well represented. The timing of the maximum reproduced by

290

the model. Particularly, the simulated results clearly capture the unusual temporal patterns of storm surge anomalies for ECTS-type typhoons are indicated by the purple arrow in Figure 4a. ECTS-type's anomalies tend to rise sharply over a short period. Chaba (2004), Bert (1999), and Tapha (2019) each had a single peak in maximum storm surge anomaly, while Songda (2004), Shanshan (2006), and Goni (2015) experienced a second peak within approximately two hours before or after the time of the maximum anomaly. Additionally, the positions of the typhoon at the time of the maximum storm surge anomaly for ECTS-type typhoons are marked with a red dot in Figure 3. The maximum storm surge anomaly occurs when the typhoon approaches NCKI. As a representative of the ECTS-type, Figure 5a shows the time series of wind and air pressure at the Fukuoka weather station during Goni (2015). The red line represents air pressure, during WCTS-type typhoons and the blue arrows indicate wind vectors. At 8:00 on August 25, 2015, when the 2-hour periodic seiche in Hakata Bay, as reported by Yamashiro et al. (2016).

5.1 Contributions of Pressure and Wind to Storm Surge Anomalies

Table 1 shows the correlation coefficient and RMSE between the storm surge anomalies simulated under combined wind and pressure forcing and the sum of the individually simulated wind-only and pressure-only cases in Hakata Bay. For all typhoons, the correlation coefficient was nearly 1, and the RMSE was extremely small.

These results indicate that the storm surge anomaly was at its maximum, the air pressure dropped to 970 hPa, and a northerly wind was blowing (indicated by the purple arrow in Figure 4a and Figure 5a). Therefore, the rapid rise in anomalies generated under simultaneous wind and pressure forcing can be decomposed into the sum of the individual surge components induced by wind and pressure, respectively—implying that the two effects act independently. In the following sections, we examine the development of storm surge anomalies under combined atmospheric pressure and wind forcing by decomposing the total surge into its pressure- and wind-driven components. We approximated the total storm surge anomaly for ECTS-type typhoons can be explained by the drop in air pressure due to the typhoon's approach, causing as the linear sum of the pressure-induced and wind-induced components, as follows:

$$\eta_{\text{pres+wind}} \approx \eta_{\text{pres}} + \eta_{\text{wind}} \quad (14)$$

where η_{pres} is the sea level to rise through the inverted barometer effect, and the northerly wind pushing seawater towards the land, further raising anomaly caused by atmospheric pressure alone, η_{wind} is the sea level anomaly caused by wind forcing alone, and $\eta_{\text{pres+wind}}$ is the sea level through wind set-up. Moreover, the appearance of a second peak during the passage of Songda (2004), Shanshan (2006), and Goni (2015) can be attributed to the fact that the peak of the static water level rise (inverted barometer effect and wind set-up) did not coincide with the peak of the 2-hour bay water oscillation in Hakata Bay (Yamashiro et al. (2016)). anomaly resulting from the combined effects of pressure and wind forcing We then investigate the specific factors contributing to the development of each component.

On the other hand, the storm surge anomaly of WCTS-type typhoons tends to show a rapid decrease in sea level after the first peak, followed by a second peak where the maximum value occurs. The red arrow in Figure 4b indicates the timing of the first peak, the blue arrow shows the timing of the sudden decrease in anomaly, and the purple arrow marks the timing of the second peak. Additionally, for WCTS-type typhoons shown in Figure 3, the green dots represent the locations of the typhoons when the first peak occurred at the Hakata tidal station, and the blue dot represents the typhoon's location when the second peak occurred. The first peak occurred when the typhoon approached Hakata Bay (Figure 3: green dot). The second peak, except in the case of Sanba (

Table 1. Correlation coefficient (R) and root mean square error (RMSE) between the simulated storm surge anomalies in Hakata Bay under combined wind and pressure forcing ($\eta_{\text{pres}+\text{wind}}$), and the sum of two separate simulations with pressure-only and wind-only forcing ($\eta_{\text{pres}} + \eta_{\text{wind}}$).

Typhoon type	Typhoon name (year)
WCTS-type	Rusa (2002)
	Maemi (2003)
	Megi (2004)
	Sanba (2012) , occurred when the typhoon entered the Sea of Japan (Figure 3: blue dot) . Figure 5b shows the time series of wind and pressure at the Fukuoka weather station.
	Chaba (2016)
	Kong-rey (2018)
	Maysak (2020)
	Haishen (2020)
Hinnamnor (2022) . The first surge peak coincided with the typhoon's closest approach to NCKI, when the minimum pressure was recorded at 991.4 hPa, thus explaining the first surge peak.	
ECTS-type	Chaba (2004)
	Songda (2004) . Thus, the second peak cannot be explained by the inverted barometer effect or wind set-up. Therefore, we aim to elucidate the mechanism behind the second surge peak.
	Shanshan (2006)
	Danas (2013)
	Goni (2015)
	Tapah (2019)

The timeseries of storm surge anomalies at the Hakata tidal station ((a) ECTS-type; (b) WCTS-type). The black line shows the observed data, and the red line is the simulated anomaly. The purple, red, and blue arrows indicate the time at which the maximum, local maximum, and local minimum is observed, respectively.

325 The time series of air pressure and winds at Fukuoka weather station. (a) ECTS-type; (b) WCTS-type.

5.2 Spatial distribution analysis

In this section, we clarify We investigated the cause and characteristics of the second peak shown in WCTS typhoons by conducting a detailed analysis of the spatial distribution of storm surge anomalies, wind, and atmospheric pressure obtained from FVCOM during Hinnamnor (2022), a representative WCTS typhoon.

330 Figure 7 illustrates shows the spatial distribution of the storm surge anomaly during Hinnamnor (2022), a representative of the WCTS-type. Panel (a) shows the storm surge anomaly when both atmospheric pressure and wind are applied as external forces $\eta_{\text{pres}+\text{wind}}$, panel (b) depicts the storm surge anomaly with only atmospheric pressure applied η_{pres} , and panel (c) presents the storm surge anomaly with only wind applied. The black dashed line represents the typhoon's track, and the star marks the typhoon's location. η_{wind} . Figure 8 shows the spatial distribution of (a) atmospheric pressure and (b) wind during the passage of Typhoon Hinnamnor (2022). The upper panels wind. The top graphs of Figure 9 show
335 the time series of the calculated tidal levels η_{pres} and η_{wind} at the Hakata Bay tidal station when the external forces of (a) pressure and (b) wind are independently applied.

At any given time, the storm surge anomaly in panel (a) of Figure 7 is the sum of the anomalies shown in panels (b) and (c) of Figure 7. In other words, for the WCTS-type, the storm surge anomaly caused by atmospheric pressure and wind are independent of each other. Therefore, by investigating the development processes of the storm surge anomaly due to atmospheric pressure and wind separately, we can consider the storm surge development mechanisms when both pressure and wind are applied
340 simultaneously.

tidal station. At 202:00 on September 6, 2022, the typhoon enters the Tsushima Strait. At this time, the sea level rises in accordance with the low-pressure according to the low air pressure distribution around the typhoon's center (Figure center (Figures 7b0 and Figure 8a0), resulting in a sea level rise of approximately 20 cm at Hakata Bay located in Hakata Bay at the center of NCKI (the NCKI (top graph in Figure 9a: upper panel). On the other hand, regarding the sea level rise caused by the wind, the storm surge). The storm
345 surge anomalies induced by winds gradually increases from NCKI towards the NCKI toward the SCKP, forming a gradient (Figure 7c0). This is because the wind is blowing towards blows toward the SCKP, causing a storm surge rise due to wind set-up an increase in storm surge anomalies due to the wind setup (Figure 8b0).

At 5At 05:00 on September 6, 2022, the typhoon was is near the SCKP, making its closest approach and at the closest point to the NCKI. At this time, with With only atmospheric pressure applied present, a positive anomaly develops around the typhoon,
350 leading to a positive anomaly throughout the Tsushima Strait (Figure 7b1). The distribution of the positive anomalies corresponds with the distribution to that of the low-pressure system (Figure 8a1). As a result, the storm surge at Hakata Bay rises anomalies in Hakata Bay increases by approximately 20 cm due to owing to the inverted barometer effect (top graph in Figure 9a: upper panel).). When wind is applied present, positive anomalies appear along the SCKP and the NCKI, although these values are relatively smaller than those at 5:00 on September 6, 2022 their values are small (Figure 7c1). The reason for this is that the wind blowing towards
355 SCKP abruptly shifted to a westerly wind as the typhoon moves northeast, disrupting the balance and causing the gradient of storm surge to begin to collapse (Figure 8b1).

By 08:00 on September 6, 2022, as the typhoon entered enters the Sea of Japan, a negative anomaly developed develops in the Tsushima Strait (Figure 7a2), which is mainly derived from wind induced the wind-induced anomaly (Figure 7c2). By 11:00 on September 6, 2022, as the typhoon continued continues northeastward in the Sea of Japan, a positive anomaly appeared appears in the NCKI (Figure 7a3), which is mainly derived from the positive anomaly induced by wind wind-induced anomaly (Figure 7c3). By 14:00 on September 6, 2022, this the positive anomaly in the NCKI intensifiedintensifies, resulting in the second peak a second peak at NCKI (Figure 7a), which is a4), mainly derived from positive anomalies induced by both air pressure and wind (FigureFigures 7b4 , and 7c4). The atmospheric pressure across the Tsushima Strait had risen to near normal reaches near-normal levels, and wind speeds were the wind speeds are below 10 m/s after 08:00 on September 6, 2022 (Figure 8a2-4, b2-4Figures 8a2–a4 and 8b2–b4). Consequently, the only forces acting on the seawater in the Tsushima Strait are gravity and the Coriolis force, with no external forces to forcibly raise notably increasing the storm surge . This second peak arises anomalies. The second peak appears from the superposition of oscillations generated in the Tsushima Strait by both atmospheric pressure and wind, with the second peak occurring in the NCKI region when the peaks of these oscillations coincide.

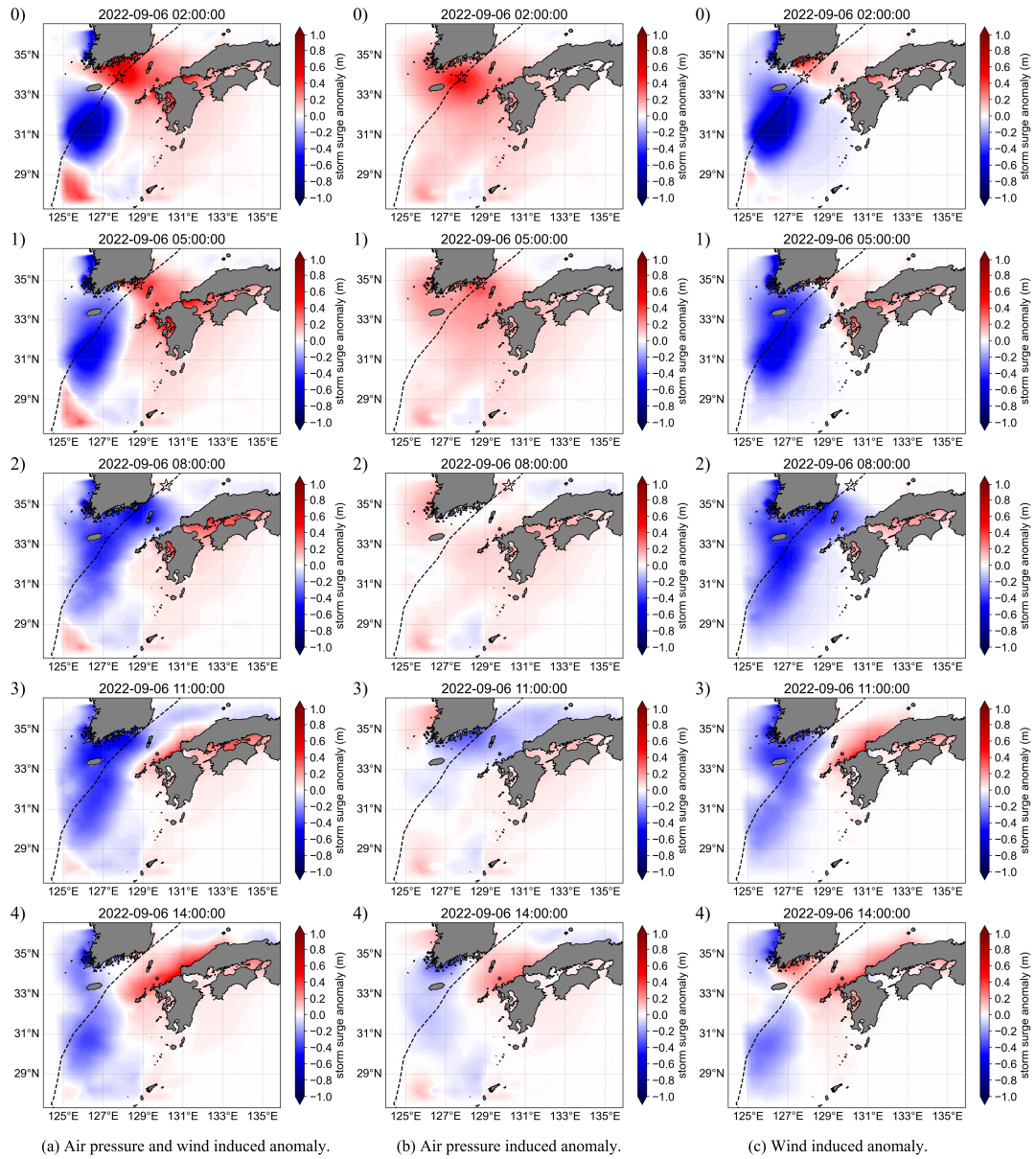


Figure 7. The distribution of storm surge anomalies during Typhoon Hinnamnor (2022). The black line shows the path of the typhoon track, and the black star indicates the position of the center of the typhoon. (a) represents the storm surge anomaly when both air resulting from the combined effects of atmospheric pressure and wind are applied as external forces, forcing ($\eta_{pres+wind}$). (b) represents the case where only air storm surge anomaly driven by atmospheric pressure is applied, and alone (η_{pres}). (c) represents the case where only storm surge anomaly driven by wind is applied forcing alone (η_{wind}).

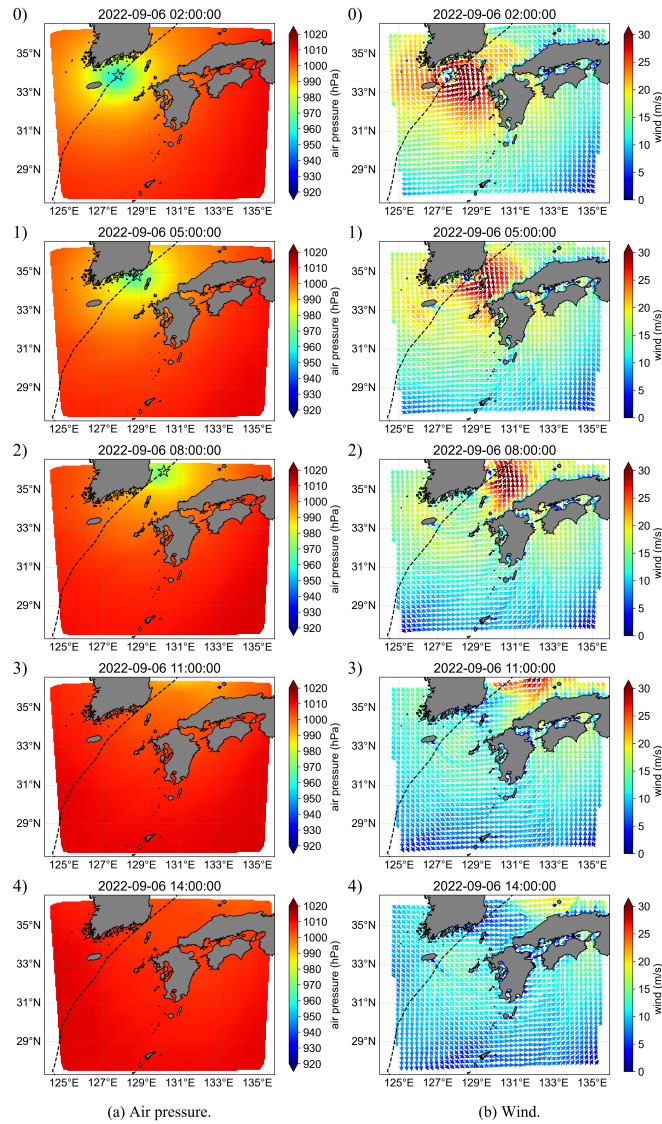


Figure 8. The distribution Distributions of (a) air pressure and (b) wind during typhoon Hinnamnor (2022). The black line shows curve indicates the path of the typhoon path, and the black star indicates the position of the center of the typhoon center. (a) represents the distribution of air pressure, and (b) represents the distribution of wind.

6 Spectral Analysis using Wavelet Transform

6.1 Continuous Wavelet Transform

370 We performed a spectral analysis using the continuous wavelet transform (CWT) to investigate oscillatory components within storm surge anomalies. The CWT is well-suited for analyzing nonstationary signals, as it enables time–frequency localization of transient features. It uses a base function, known as the mother wavelet, which is scaled and shifted to compare with the signal of interest, allowing for frequency decomposition over time. The mother wavelet is given by

$$\psi_{a,b}(t) = \frac{1}{\sqrt{a}} \psi\left(\frac{t-b}{a}\right) \quad (15)$$

375 where $\psi(t)$ is the mother wavelet, t denotes time, a is the scale, and b is the shift. When a increases, the mother wavelet stretches, making it more suitable for analyzing long waves. An increase in b results in a parallel shift in the positive direction along the time axis. For the mother wavelet defined by scale a and shift b , denoted by $\psi_{a,b}(t)$, the CWT is defined as

$$W_{\psi_{a,b}}[x(t)] = \int_{-\infty}^{\infty} x(t) \psi_{a,b}^*(t) dt \quad (16)$$

380 where $x(t)$ is the signal of interest and $*$ denotes the complex conjugate. By continuously varying scale a and shift b , the CWT is a mapping onto a two-dimensional plane of (a, b) , allowing frequency analysis in the time domain. We use the following complex Morlet wavelet as the mother wavelet:

6.2 Mechanism of storm surge development

6.1.1 Wavelet transform

385
$$\psi(t) = \frac{1}{\sqrt{\pi B}} \exp\left(-\frac{t^2}{B}\right) \exp(2\pi Cjt) \quad (17)$$

where j is the imaginary unit, $B = 1.5$ is the bandwidth, and $C = 1.0$ is the center frequency. These values are recommended and lead to a high resolution and reduced artifacts (Lee et al. (2019)).

This chapter discusses the factors contributing

6.2 Dominant Oscillation Modes Identified by CWT

390 We analyze the factors that contribute to the second peak during the passage of a WCTS-type WCTS typhoon. As shown in Figure 4 and 7, the storm surge anomaly fluctuates due to because of the superposition of oscillations with multiple periods. To identify the oscillatory components other than tidal constituents present in the storm surge anomaly time series in the time series of storm surge anomalies in Hakata Bay, continuous wavelet transform (CWT) is applied. The lower panels of the CWT was applied. The lower graphs in Figure 9 present the results of the continuous wavelet transform, referred to as CWT scalograms, where atmospheric pressure

395 (panel a) and wind (panel b) are applied independently independently imposed as external forces. In both (a) and (b), three types of
Figure 10 shows the time series of these oscillatory components—2, 5, and 10 hours—extracted using the inverse CWT.

In both cases, three dominant oscillations with periods of 10 h, 5 h, and 2 h are observed. Figure 10 shows the timeseries of oscillatory
components with periods of 2 h, 5 h, and hours are observed from 05:00 on September 6, 2022 to 17:00 on September 7, 2022. The 2-
hour oscillation component has a maximum amplitude of approximately 10 h in Hakata Bay by inverted CWT. The red line represents the case
400 where atmospheric pressure is the external force, while the blue line represents the case where wind is the external force. The 2-h period oscillation is a harbor oscillation at
Hakata Bay (Yamashiro et al. (2016)). This oscillation occurred both before the typhoon approached Hakata Bay and after it passed over cm, regardless of whether
the external forcing is atmospheric pressure or wind, and the times of maximum amplitude coincided ((Figure 10a).
Meanwhile, when atmospheric pressure is applied as the external force, the 5-h period oscillation reaches its maximum amplitude at 13:00 on September 6, 2022 (Figure 10b:
cal_p). When wind is the external force, this maximum amplitude occurs). On the other hand, for the 5- and 10-hour oscillations, the maximum
405 amplitude for the 5-hour oscillation ranges from 10 to 15 cm, with wind forcing resulting in an amplitude approximately 1.5
times larger than that caused by atmospheric pressure. The phase of the 5-hour oscillation is also about 2 h earlier, at 11:00
on September 6, 2022 hours earlier under wind forcing (Figure 10b: cal_w). In both cases, when atmospheric pressure and wind are the external forces,
the 5-h period oscillation coincides with the second peak in the storm surge anomaly, following a minimum.).

Similarly, for the 10-h period 10-hour oscillation, the peak occurs about approximately 2 h earlier when hours earlier when
410 the wind is the external force (Figure 10c). The maximum amplitude is reached observed between 11:00 and 17:00 on
September 6, 2022, corresponding which corresponds to the second peak in of the storm surge anomaly, with the oscillation continuing
afterward at a decreasing amplitude. Figure after which the amplitude gradually decreases. Compared to the 5-hour oscillation, the
10-hour oscillation component persists for a longer duration.

Figures 11 and Figure 12 show the spatial distribution of the 5-h and 10-h distributions of the 5 and 10-hour period oscillatory
415 components in the Tsushima Strait, respectively. For the 5-h 5-hour period oscillation, regardless of the external force, the
Tsushima Island, the boundary between the East China Sea and the Tsushima Strait, and the boundary Tsushima Strait and that
between the Sea of Japan and the Tsushima Strait act as nodes, while the SCKP and the NCKI serve as antinodes.
Additionally, In addition, the SCKP and NCKI cells are in opposite phases. The timing of the oscillation differs depending depends
on the external force: when. When atmospheric pressure is the external force (Figure 11a), the oscillation begins at 7:07:00
420 on September 6, 2022, when the typhoon is located on the eastern coast of Korea; when. When wind is the external force
(Figure 11b), the oscillation starts at 5:05:00 on September 6, 2022, as when the typhoon is located near the SCKP, with
wind forcing the wind force occurring 2h earlier. For the 10-h hours earlier.

For the 10-hour period oscillation, the boundary between the East China Sea and the Tsushima Strait, and the boundary Tsushima
Strait and that between the Sea of Japan act as nodes, while the Tsushima Island, the SCKP, and the NCKI serve as
425 antinodes. Unlike the 5-h 5-hour period oscillation, the SCKP and NCKI are in the same phase. The timing of the 10-h
10-hour period oscillation is similar to that of the 5-h 5 h period oscillation, with wind forcing force occurring 2 h hours earlier.

Considering that both atmospheric pressure and wind had returned to normal conditions by the time the 5-h and 10-h period oscillations occurred at the NCKI, these
oscillations are likely driven by the natural frequencies induced by the topography seiche rather than by external forces. It can be inferred that the second peak in the storm
surge anomaly is a result of the superposition of these two oscillatory components.

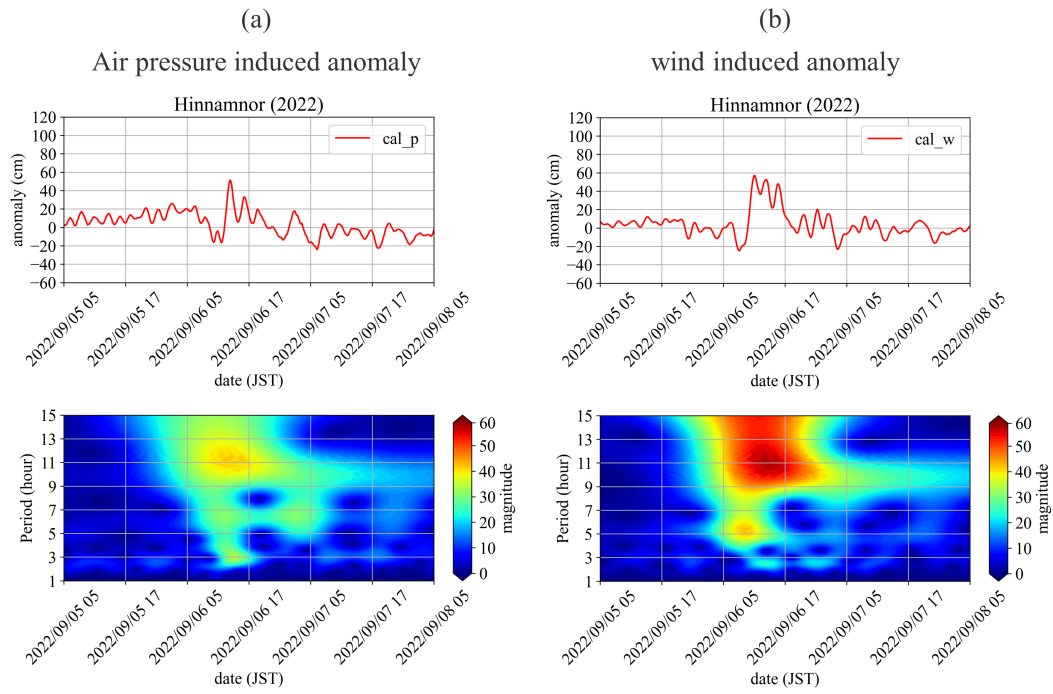


Figure 9. Simulated time series and scalograms at the Hakata tidal station . for anomalies induced by (a) shows the case where the anomaly induced by air pressure is transformed, and (b) shows the case where the anomaly induced by wind is transformed.

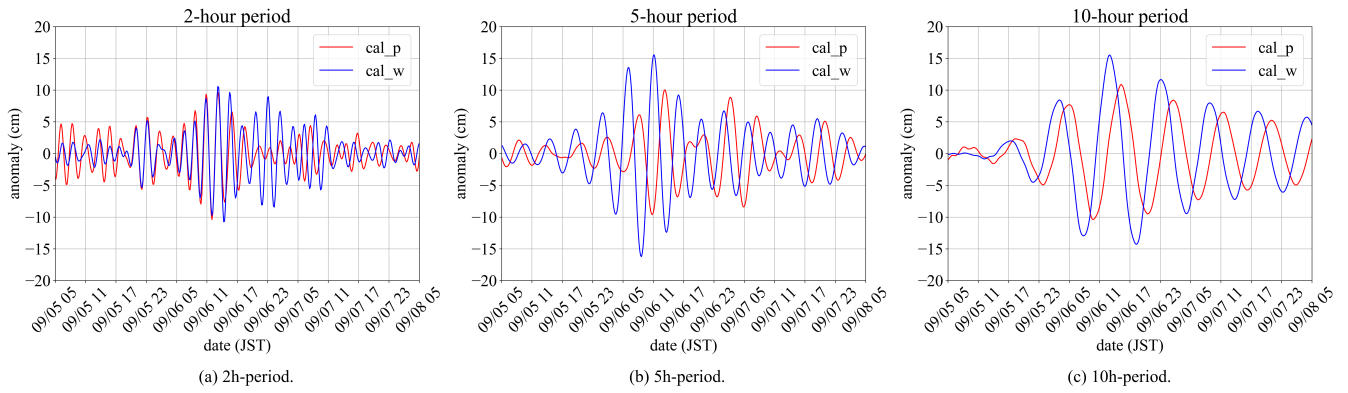


Figure 10. Timeseries Time series of oscillatory components with periods of (a) 2 hours, (b) 5 h, and (c) 10 h at the Hakata tidal station obtained by inversed inverse CWT. The red and blue lines show curves indicate the anomalies induced by air pressure and wind-induced anomalies, respectively.

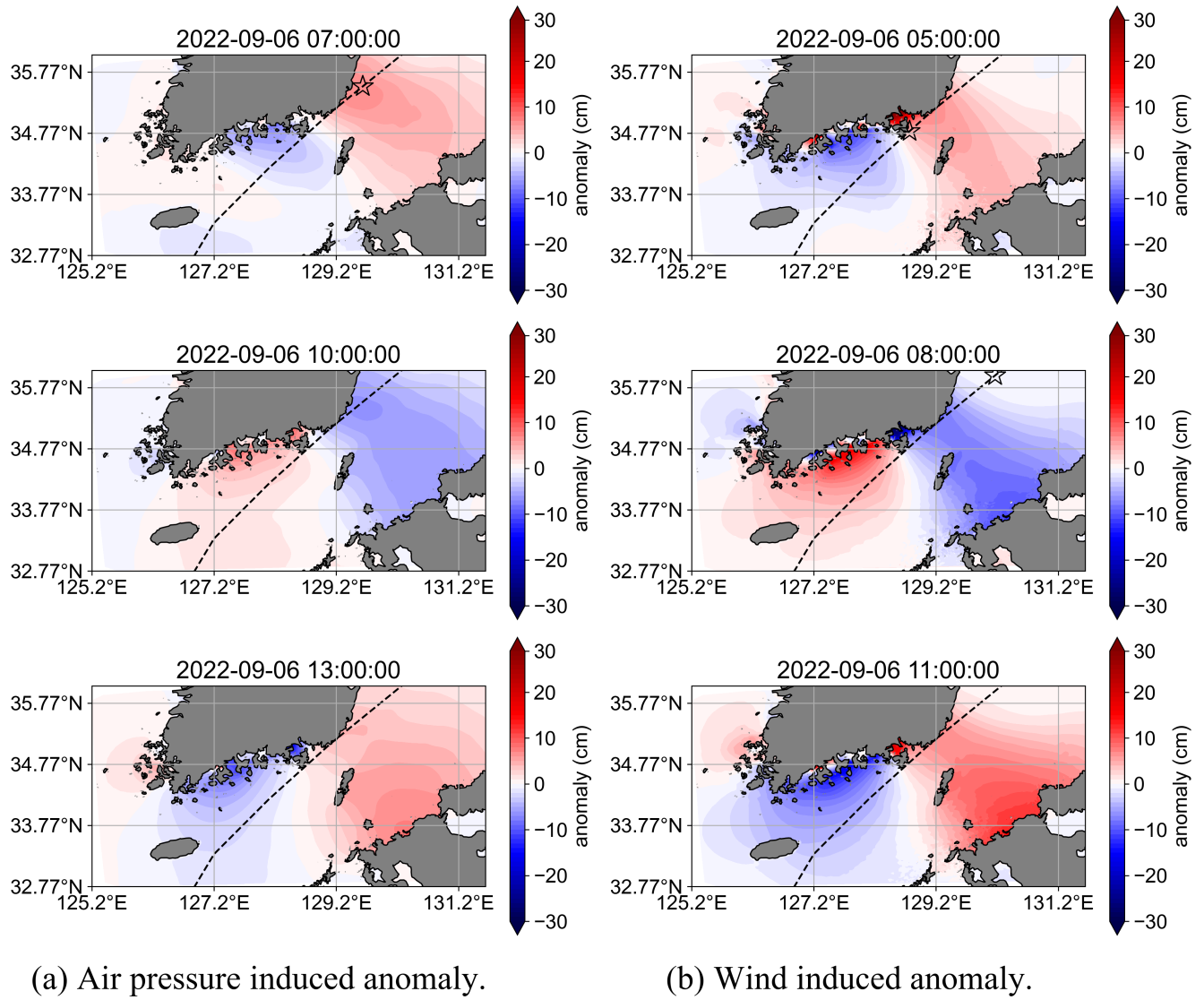


Figure 11. The distribution of 5-h period oscillations in Tsushima Strait for anomalies induced by (a) air pressure and (b) wind.

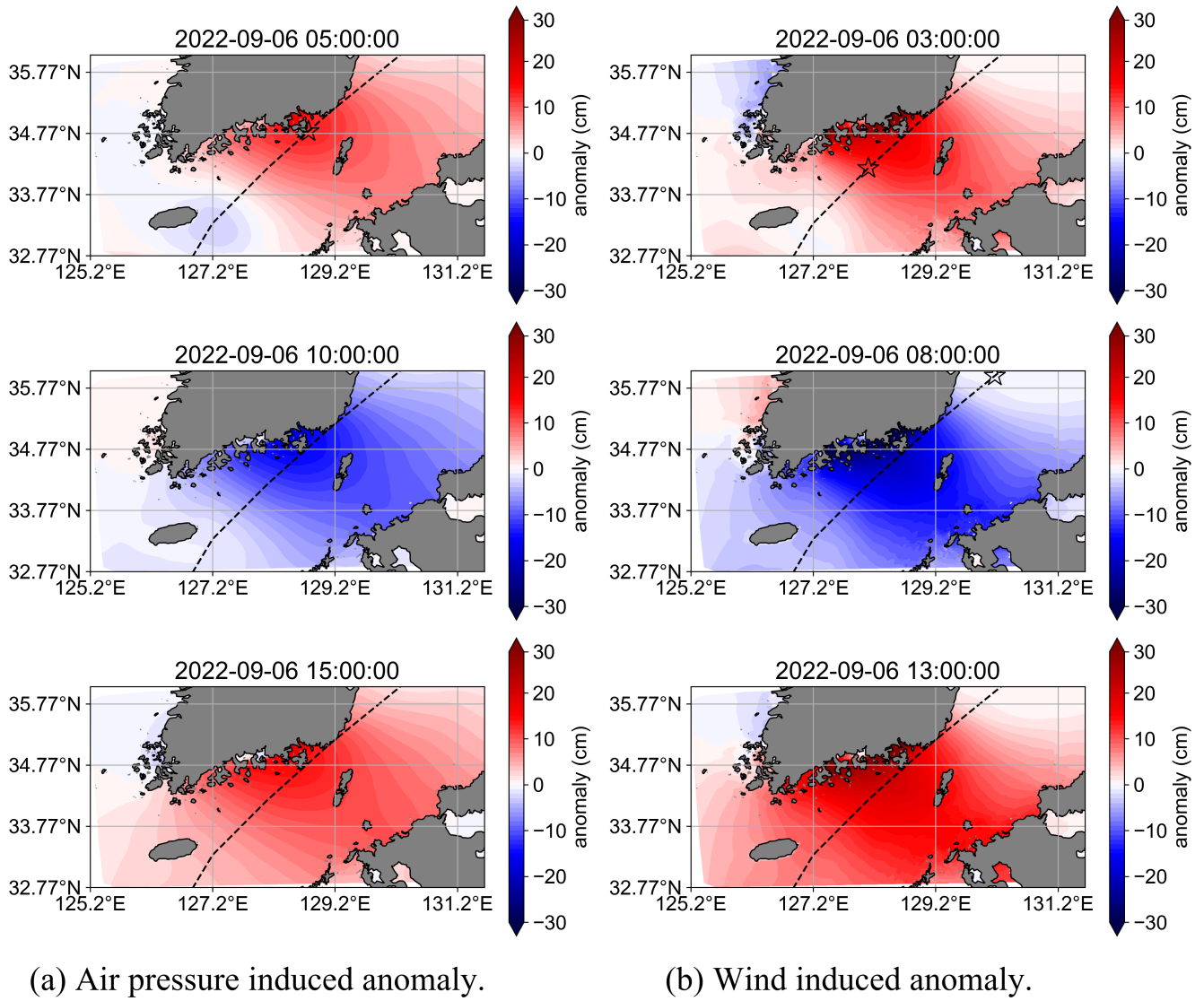


Figure 12. The distribution of 10-h period oscillations in Tsushima Strait for anomalies induced by (a) air pressure and (b) wind.

The reason both the 5-h and 10-h period oscillations form nodes at the boundaries between the Tsushima Strait and the

7 Discussion

The timing of oscillation generation differs between external forces as shown in Figures 11 and 12. This is owing to variations in the constraint-removal timing. In the pressure-only case, the storm surge anomalies along the SCKP reached its maximum at 05:00 on September 6, 2022, when the typhoon was closest to the SCKP (Figures 7b1 and 8a1). After this point, as the typhoon moved into the Sea of Japan, as well as between the Tsushima Strait and the East China Sea, is due to the rapid increase in water depth. external forcing diminished, and oscillations with 10-hour and 5-hour periods began to develop. In contrast, in the wind-only case, the maximum storm surge anomaly along the SCKP occurred earlier, at 02:00 on September 6, 2022 (Figures 7c0 and 8b0), a few hours before the typhoon reached its closest approach. This is because, at that time, the wind was directed toward the SCKP, generating a strong wind setup and resulting in a significant storm surge at the SCKP. As the typhoon reached its closest to the SCKP at 05:00, the wind direction shifted substantially, releasing the constraint on the water and initiating oscillatory motion. Therefore, in the wind-only case, the external forcing was released earlier than in the pressure-only case, leading to an earlier onset of oscillations. As the total storm surge anomaly is represented as the linear sum of the pressure-induced and wind-induced components, the NCKI experiences a higher and more prolonged storm surge compared to the cases with only one forcing component (Figures 7a3 and a4).

As shown in Figure 1b, there is a significant large change in water depth at these boundaries the boundary between the Tsushima Strait and Sea of Japan. When such a discontinuous change in the water depth occurs, it is known that the amplitude of the oscillations decreases exponentially near the discontinuity. For example, the waveform of the edge waves when the water depth changes discontinuously is described by the following equation. as follows:

$$450 \quad \eta_1 = a \cos(\mu_1 x) \cos(ky + \sigma t) \quad (18)$$

$$\eta_2 = a \cos(\mu_1 l) e^{-\mu_2(x-l)} \cos(ky + \sigma t) \quad (19)$$

$$\mu_1 = \sqrt{\frac{\sigma^2}{gh_1} - k^2}, \quad \mu_2 = \sqrt{k^2 - \frac{\sigma^2}{gh_2}} \quad (20)$$

Let the coastline lie along the y -axis, with $x > 0$ representing the sea. The water depth and width of the continental shelf are denoted as h_1 and l , respectively, while the . The water depth of the deep sea is h_2 , with where $h_1 < h_2$ (i.e., the depth of the deep sea is greater than that of the continental shelf). The wave-number wave number and angular frequency are represented by k and σ , respectively, and where $a > 0$ is a constant. According to Equation (19), the oscillation amplitude in the region where $x > l$ (the i.e., deeper area) becomes significantly smaller compared to substantially smaller than that in the region where $x < l$ due to because of the discontinuous change in the water depth.

This phenomenon arises from because of the properties of long waves. The group velocity of long waves is expressed as $C = \sqrt{gh}$, meaning indicating that waves move slower more slowly in shallow regions and faster in deeper regions. As a

Consequently, when long waves generated in shallow areas attempt to enter deeper regions, they propagate toward deeper areas, their group velocity increases rapidly. This sudden shift in velocity disrupts the wave's penetration into the deeper water, causing part due to the depth transition. This abrupt change in wave speed hinders the efficient transmission of wave energy into deeper waters, resulting in partial reflection of the incoming wave to reflect as if waves—similar to encountering a fixed boundary at the point where the water depth changes depth discontinuity. The interaction between the reflected and incoming waves forms gives rise to standing waves, creating establishing a fluid oscillatory system where specific oscillation periods dominate. Consequently, dominated by specific natural oscillation periods.

Consequently, oscillations do not occur in much deeper regions, oscillations do not occur, leading to the formation of nodes. This explains why the 5-h and 10-h leading to node formation. Hence, the 5 and 10 h period oscillations are confined to the shallow regions, where these standing wave patterns develop.

Here, we examine the reasons behind the 5-h period oscillation creating a node in the region between the SCKP and the NCKI, near NCKI near the Tsushima Island. This phenomenon is related to the oscillation mode oscillation without the Coriolis force. By solving the wave equation, we obtain

$$\frac{\partial^2 \eta}{\partial t^2} = c^2 \left(\frac{\partial^2 \eta}{\partial x^2} + \frac{\partial^2 \eta}{\partial y^2} \right) \quad (21)$$

$$c = \sqrt{gh} \quad (22)$$

in a rectangular domain with dimensions $b \times l$, where the depth h is constant, and ensuring and ensures that the solution satisfies the following boundary conditions:

$$v = 0, \quad (y = 0, b) \quad (23)$$

$$\eta = 0, \quad (x = 0, l) \quad (24)$$

The following solution is obtained:

$$\eta = A \sin(kx) \cos(k'y) \sin(\sigma t) \quad (25)$$

$$k = \frac{m}{l} \pi, \quad k' = \frac{n}{b} \pi, \quad \sigma = c \sqrt{k^2 + k'^2} \quad (26)$$

Here, where m and n are integers representing the modes of vibration vibration modes in the x -axis - and y -axis directions, respectively. Additionally, the period of oscillation oscillation period is given by

$$T_{m,n} = \frac{2\pi}{\sigma} = \frac{2}{\sqrt{gh}} \left\{ \left(\frac{m}{l} \right)^2 + \left(\frac{n}{b} \right)^2 \right\}^{-1/2} \quad (27)$$

For the spatial scale of the Tsushima Strait, with $h = 80$ m, $l = 550$ km, $b = 250$ km, and $A = 5$ cm, the solutions for $(m, n) = (1, 1), (1, 0)$ are presented in Equation (25) and depicted in Figure 13. The oscillation with $(m, n) = (1, 1)$ has nodes at $x = 0$ and l , $y = \frac{b}{2}$, and antinodes at $x = \frac{l}{2}$, $y = 0$ and b . The oscillation with $(m, n) = (1, 1)$ has nodes at $x = 0$ and l , and $y = \frac{b}{2}$, and antinodes at $x = \frac{l}{2}$, and $y = 0$ and b . The period of this oscillation is $T_{1,1} = 4.52$ h. Additionally, In addition,

490 the oscillation with $(m, n) = (1, 0)$ has nodes at $x = 0$ and l , and antinodes at $x = \frac{l}{2}$. The period of this oscillation is $T_{1,0} = 10.91$ h. These periods correspond to the 5-h and 10-h 5 and 10 h periods observed in the CWT.

Therefore, during the passage of WCTS-type typhoons, there are two peaks in storm surge at the NCKI (Figure 4b: red arrow and purple arrow). The first peak can be attributed to the barometer effect (Figure 7b1 and 8a1). As the typhoon progresses into the Sea of Japan, the constraints from wind set-up and the barometer effect are alleviated, releasing potential energy and resulting in oscillations with periods of approximately 5 h in the $(1, 1)$ mode and and show that these oscillations
495 cause delayed storm surges. The sea level differences observed at Izuhara (located on Tsushima Island) and Busan (in SCKP) during typhoon passages through the strait, as reported by Yi (1970), are likely associated with the 10 h in the $(1, 0)$ mode (Figure 11 and 12). The timing of oscillation generation differs between external forces such as atmospheric pressure and wind due to the variation in constraint removal timing. For atmospheric pressure, and 5-hour period oscillation modes.

The above discussion was conducted under the assumption of no Coriolis force; however, Wu et al. (2021) demon-
500 strated that the tidal dynamics (K2 and M2) in the Tsushima Strait are primarily governed by Kelvin waves and partial reflection of Kelvin waves occurs at the peak water level at the SCKP occurs when the typhoon is directly overhead on SCKP (Figure 7b1 and 8a1). In contrast, for wind, the peak water level occurs when the prevailing southeast wind at the SCKP causes the maximum onshore push, which happens earlier (Figure 7c0 and 8b0). By the time the peak water level due to atmospheric pressure is reached, the constraint from wind has already been released, leading to earlier onset of oscillations due to wind. That is why the second peak in storm surge
505 junction between the Tsushima Strait and the Japan Sea. The identified oscillations propagated with the coastline on their right, which is consistent with the typical propagation direction of Kelvin waves in the Northern Hemisphere. This suggests that the observed oscillatory behavior is strongly influenced by the characteristics of Kelvin waves. Niimi et al. (2022) compared numerical simulations of Typhoon Maysak (2020) with and without the Coriolis force and found that the second storm surge peak at the NCKI results from the superposition of these two oscillation modes. was significantly reduced when the Coriolis force was excluded. Notably, the 10-hour oscillation component still
510 appeared even in the absence of the Coriolis force; however, the 5-hour oscillation component vanished. This indicates that the 5-hour oscillation identified through continuous wavelet transform (CWT) analysis is highly sensitive to and likely governed by the Coriolis force.

In Typhoon Hinnamnor (2022), the second peak is well-explained by the superposition of the $(1, 1)$ and $(1, 0)$ mode oscillations. However, in cases Furthermore, among WCTS-type typhoons, those that travel northward through the Tsushima Strait—such as Maysak (2020) and
515 Haishen (2020), where high tidal deviations persisted long after the second peak (Figure 4), it was observed that the —tend to produce a second storm surge peak that is both larger and longer-lasting. This is likely due to the continued southwesterly winds following these typhoons caused Ekman transport, pushing seawater toward the NCKI (Niimi et al. (2022)). This results in a situation where the water level remains elevated even after the second peak. Prolonged high storm surge increases the probability of occurring high astronomical tides and high storm surge at the same time, raising the risk of flooding. Typhoons that maintain high water levels after the second peak are often those moving north through the Tsushima Strait within the WCTS-type category (Figure 3).
520 It is believed that even minor differences in their paths the typhoon's passage, which induced Ekman transport. Even minor variations in typhoon tracks can lead to variations differences in the persistence of storm surge deviations. Future research will focus on identifying anomalies. In future research, we aim to identify WCTS-type typhoons that generate the most dangerous hazardous storm surges by considering the combined effects of Ekman transport, oscillations in the $(1, 1)$ and $(1, 0)$ $(1, 1)$ and $(1, 0)$ modes, and the timing of the release of external forces forcing.

525 Given the potential for the delayed storm surges caused by WCTS-type typhoons, even after an first peak in water levels, it's crucial that we don't prematurely assume safety. Therefore, we believe it's essential to implement measures that extend the period during which people remain evacuated, preventing them from returning home too soon. Moreover, future climate change, characterized by increased typhoon intensity and sea-level rise, could lead to unforeseen inundation in areas previously unaffected. Therefore, to prepare for such flooding, it's crucial for the relevant coastal regions to take
530 measures. These include elucidating the mechanisms of water level rise and establishing predictive methods for these phenomena.

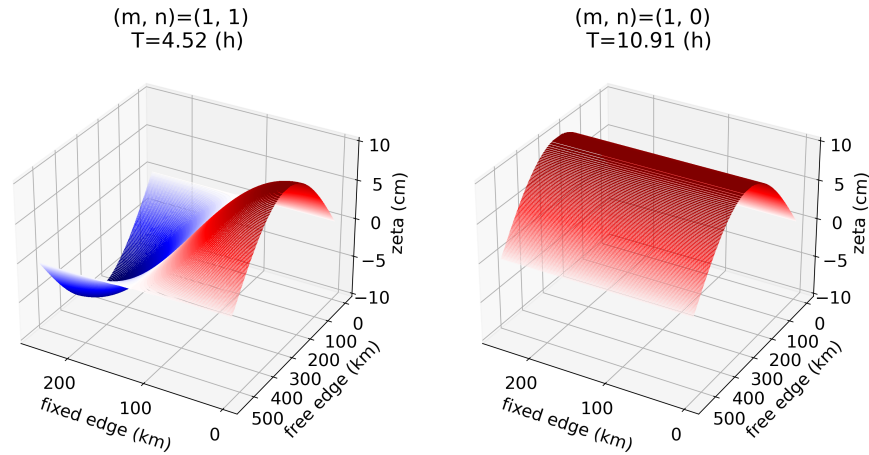


Figure 13. Solutions of the wave equation, where m and n represent the mode of vibration in the free edge direction and fixed edge direction, respectively. Color corresponds to the zeta value.

8 Conclusions

This study

In this study, we investigated the mechanisms of behind storm surge development at along the NCKI using observational data, storm surge numerical simulations, and continuous wavelet transforms CWT. Typhoons that cause significant storm surges at induce large storm surges in the NCKI can be classified categorized based on their paths: one type passes from ECTS to NCKI, and the other passes tracks—either approaching from the ECTS or from the SCKP through the WCTS.

For ECTS-type typhoons, when the storm storm surge peaks occur when the typhoon is closest to NCKI, the pressure drops to its lowest, and north winds push seawater towards NCKI, causing the storm surge peak. Therefore, the storm surge development process for ECTS-type typhoons can be the NCKI. At this point, atmospheric pressure reaches its minimum, and northerly winds drive seawater toward the coast, resulting in a surge. This behavior is well explained by the inverted barometer effect and wind set-up setup. In contrast, WCTS-type typhoons cause an initial peak in storm surge at the time of the closest approach, display a more complex pattern. The storm surge initially peaks as the typhoon nears the NCKI, then rapidly declines, followed by a rapid decrease. However, a second peak in storm surge, which is larger than the first, occurs later, resulting in a significant storm surge at NCKI second, larger peak after the typhoon has passed. By At the time of the this second peak, atmospheric pressure has returned to near-normal levels and wind speeds are low, rendering typical storm surge mechanisms—such as the barometer effect and wind set-up insufficient to explain this phenomenon setup—inadequate to explain the surge.

Spectral analysis using continuous wavelet transforms the CWT revealed a continuous 2-h periodic oscillation, with oscillations of 5-h and 10-h periods emerging after the first peak. The 2-h period oscillation is localized to Hakata Bay. 2-hour periodic oscillation localized in Hakata Bay, along with the emergence of 5- and 10-hour oscillations following the initial surge peak. To investigate the characteristics of the 5-h spatial characteristics of these longer-period oscillations, we conducted storm surge simulations and 10-h period oscillations, storm surge numerical simulations were performed, and spectral analysis was conducted on the obtained spatial distributions using continuous wavelet transforms. The 5-h period oscillation, characterized by antinodes at NCKI applied CWT analysis to the resulting spatial data. The 5-hour oscillation, with antinodes at the NCKI and SCKP and the SCKP and nodes a node at Tsushima Island, represents the (1, 1) mode of the Tsushima Strait's natural oscillation. The 10-h period oscillation located in the center of the strait, corresponds to the (1, 0) (1, 1) natural oscillation mode of the Tsushima Strait's natural oscillation. The 10-hour oscillation represents the (1, 0) mode. These oscillations arise from are triggered by the release of potential energy in the Tsushima Strait when the typhoon enters the Japan Sea. The stored within the strait after the typhoon exits into the Sea of Japan. The 5-hour mode appears to be strongly influenced by the Coriolis force, as suggested by prior numerical experiments. The superposition of these two mode oscillations (1, 0) and (1, 1) modes leads to the delayed second peak in storm surge at NCKI observed in NCKI storm surges.

We identified the occurrence of anomalous storm surges caused by an anomalous storm surge phenomenon associated with typhoons passing through a strait semi-enclosed straits under specific conditions and conducted a detailed investigation of their generation mechanisms. the underlying mechanisms. Our findings emphasize the critical role of resonance effects in such straits, offering new insights into storm surge risks under particular typhoon scenarios. These mechanisms are not limited to the studied region; they can occur in any area unique to the Tsushima Strait and may occur in other regions where typhoons or low-pressure systems

pass through a strait . However, it is important to note that the similar strait geometries. Importantly, variations in oscillation period, amplitude, and the components contributing to the oscillations vary, leading to modal structure can lead to differences in the timing and magnitude of storm surges . across different locations. Future climate change, with increased typhoon intensity and sea-level rise, may cause unexpected flooding in previously unaffected areas. Therefore, it's crucial for coastal regions to
570 prepare by understanding the mechanisms of water level rise and developing predictive methods.

Code and data availability. The datasets and files analyzed during the current study are available from the corresponding author upon reasonable request.

Author contributions. Conceptualization, Shinichiro Ozaki, Yoshihiko Ide and Masaru Yamashiro; Data curation, Shinichiro Ozaki; Formal analysis, Shinichiro Ozaki; Funding acquisition, Shinichiro Ozaki; Investigation, Shinichiro Ozaki and Yoshihiko Ide; Methodology,
575 Shinichiro Ozaki and Yoshihiko Ide; Project administration, Masaru Yamashiro; Resources, Shinichiro Ozaki; Software, Shinichiro Ozaki and Yoshihiko Ide; Supervision, Yoshihiko Ide and Masaru Yamashiro; Validation, Shinichiro Ozaki; Visualization, Shinichiro Ozaki; Writing – original draft preparation, Shinichiro Ozaki; Writing – review editing, Shinichiro Ozaki, Yoshihiko Ide and Masaru Yamashiro. All authors have read and agreed to the published version of the manuscript.

Competing interests. The authors declare that they have no known competing financial interests or personal relationships that could have
580 appeared to influence the work reported in this paper.

Acknowledgements. This work was supported by JST BOOST, Japan under Grant Number JPMJBS2406.

Declaration of generative AI and AI-assisted technologies in the writing process

During the preparation of this work, the authors used Chat GPT in order ChatGPT to improve language. After using this tool, the authors reviewed and edited the content as needed and . The authors take full responsibility for the content of the
585 publication.

References

- Balaguru, K., Judi, D., and Leung, L.: Future hurricane storm surge risk for the U.S. gulf and Florida coasts based on projections of thermodynamic potential intensity, *Climatic Change*, 138, 99–110, <https://doi.org/10.1007/s10584-016-1728-8>, 2016.
- Bhaskaran, P. K., Rao, A. D., and Murty, T.: Tropical Cyclone–Induced Storm Surges and Wind Waves in the Bay of Bengal, pp. 237–294, <https://doi.org/https://doi.org/10.1002/9781119359203.ch17>, 2020.
- 590
- Bilskie, M. V., Hagen, S. C., Medeiros, S. C., Cox, A. T., Salisbury, M., and Coggin, D.: Data and numerical analysis of astronomic tides, wind-waves, and hurricane storm surge along the northern Gulf of Mexico, *Journal of Geophysical Research: Oceans*, 121, 3625–3658, <https://doi.org/https://doi.org/10.1002/2015JC011400>, 2016.
- Chen, C., Liu, H., and Beardsley, R. C.: An Unstructured Grid, Finite-Volume, Three-Dimensional, Primitive Equations Ocean Model: Application to Coastal Ocean and Estuaries, *Journal of Atmospheric and Oceanic Technology*, 20, 159 – 186, [https://doi.org/10.1175/1520-0426\(2003\)020<0159:AUGFVT>2.0.CO;2](https://doi.org/10.1175/1520-0426(2003)020<0159:AUGFVT>2.0.CO;2), 2003.
- 595
- Hong, C.-H. and Yoon, J.-H.: The Effect of Typhoon on the Coastal Sea Level Variations in the Tsushima Straits, *Oceanography in Japan*, 1, 225–249, <https://doi.org/10.5928/kaiyou.1.225>, 1992.
- Ide, Y., Kora, T., Kodama, M., Yamashiro, M., and Hashimoto, N.: LONG-TERM PROJECTION OF STORM SURGE CHARACTERISTICS IN SUO-NADA SEA USING LARGE ENSEMBLE CLIMATE PROJECTION DATA, *Journal of Japan Society of Civil Engineers, Ser. B3 (Ocean Engineering)*, 76, I_1091–I_1096, https://doi.org/10.2208/jscejoe.76.2_I_1091, (in Japanese)., 2020.
- 600
- Igarashi, Y. and and, Y. T.: Application of recurrent neural network for prediction of the time-varying storm surge, *Coastal Engineering Journal*, 63, 68–82, <https://doi.org/10.1080/21664250.2020.1868736>, 2021.
- Kennedy, A. B., Gravois, U., Zachry, B. C., Westerink, J. J., Hope, M. E., Dietrich, J. C., Powell, M. D., Cox, A. T., Luettich Jr, R. A., and Dean, R. G.: Origin of the Hurricane Ike forerunner surge, *Geophysical Research Letters*, 38, 2011.
- 605
- Kim, S., Matsumi, Y., Yasuda, T., and Mase, H.: Mechanism of Abnormal Storm Surges after Passage of Typhoons around West Coasts of the Sea of Japan, *Journal of Japan Society of Civil Engineers, Ser. B2 (Coastal Engineering)*, 66, 221–225, <https://doi.org/10.2208/kaigan.66.221>, (in Japanese)., 2010.
- Large, W. G. and Pond, S.: Open Ocean Momentum Flux Measurements in Moderate to Strong Winds, *Journal of Physical Oceanography*, 11, 324 – 336, [https://doi.org/10.1175/1520-0485\(1981\)011<0324:OOMFMI>2.0.CO;2](https://doi.org/10.1175/1520-0485(1981)011<0324:OOMFMI>2.0.CO;2), 1981.
- 610
- Lee, G. R., Gommers, R., Waselewski, F., Wohlfahrt, K., and O’Leary, A.: PyWavelets: A Python package for wavelet analysis, *Journal of Open Source Software*, 4, 1237, <https://doi.org/10.21105/joss.01237>, 2019.
- Mellor, G. L. and Yamada, T.: Development of a turbulence closure model for geophysical fluid problems, *Reviews of Geophysics*, 20, 851–875, 1982.
- 615
- Miguel Esteban, Takahito Mikami, T. S. H. T. S. N. J. M. v. L.: CLIMATE CHANGE ADAPTATION IN TOKYO BAY: THE CASE FOR A STORM SURGE BARRIER, *Coastal Engineering Proceedings*, 1, management.35, <https://doi.org/10.9753/icce.v34.management.35>, 2014.
- Mori, S., Shimura, T., Miyashita, T., Webb, A., and Mori, N.: Future changes in extreme storm surge based on a maximum potential storm surge model for East Asia, *Coastal Engineering Journal*, 64, 630–647, <https://doi.org/10.1080/21664250.2022.2145682>, 2022.
- 620
- Nakajo, S., Fijiki, H., Kim, S., Mori, N., Shibutani, Y., and Yasuda, T.: AN PARAMETRIC STUDY ON POTENTIAL OF STORM SURGE IN TOKYO BAY, *Journal of Japan Society of Civil Engineers, Ser. B2 (Coastal Engineering)*, 71, I_199–I_204, https://doi.org/10.2208/kaigan.71.I_199, (in Japanese)., 2015.

- Niimi, M., Ide, Y., Yamashiro, M., Hashimoto, N., and Kodama, M.: A CASE STUDY OF STORM SURGE INUNDATION IN DOKAI BAY BY TYPHOON MAYSACK IN 2020 AND ITS GENERATION MECHANISM, *Journal of Japan Society of Civil Engineers, Ser. B2 (Coastal Engineering)*, 78, I_217–I_222, https://doi.org/10.2208/kaigan.78.2_I_217, (in Japanese), 2022.
- Shen, J. and Gong, W.: Influence of model domain size, wind directions and Ekman transport on storm surge development inside the Chesapeake Bay: A case study of extratropical cyclone Ernesto, 2006, *Journal of Marine Systems*, 75, 198–215, 2009.
- Smagorinsky, J.: General circulation experiments with the primitive equations: I. The basic experiment, *Monthly weather review*, 91, 99–164, 1963.
- 630 Soontiens, N., Allen, S. E., Latornell, D., Souëf, K. L., Machuca, I., Paquin, J.-P., Lu, Y., Thompson, K., and Korable, V.: Storm Surges in the Strait of Georgia Simulated with a Regional Model, *Atmosphere-Ocean*, 54, 1–21, <https://doi.org/10.1080/07055900.2015.1108899>, 2016.
- Tkalich, P., Vethamony, P., Babu, M. T., and Malanotte-Rizzoli, P.: Storm surges in the Singapore Strait due to winds in the South China Sea, *Natural Hazards*, 66, 1345–1362, <https://doi.org/10.1007/s11069-012-0211-8>, 2013.
- 635 Walton, T. and Dean, R.: Influence of discrete step size on wind setup component of storm surge, *Coastal Engineering*, 56, 1005–1008, <https://doi.org/10.1016/J.COASTALENG.2009.05.003>, 2009.
- Wu, D., Fang, G., Wei, Z., and Cui, X.: Study of the tidal dynamics of the Korea Strait using the extended Taylor method, *Ocean Science*, 17, 579–591, <https://doi.org/10.5194/os-17-579-2021>, 2021.
- Wu, G., Shi, F., Kirby, J. T., Liang, B., and Shi, J.: Modeling wave effects on storm surge and coastal inundation, *Coastal Engineering*, 640, 371–382, 2018.
- Wunsch, C. and Stammer, D.: Atmospheric loading and the oceanic “inverted barometer” effect, *Reviews of Geophysics*, 35, 79–107, 1997.
- Yamashiro, M., Sonoda, A., Yurino, A., Kubo, T., Yokota, M., and Hashimoto, N.: STUDY ON BASIC CHARACTERISTICS OF STORM SURGE IN HAKATA BAY, *Journal of Japan Society of Civil Engineers, Ser. B3 (Ocean Engineering)*, 72, I_348–I_353, 645 https://doi.org/10.2208/jscejoe.72.I_348, (in Japanese), 2016.
- Yang, J.-A., Kim, S., Son, S., Mori, N., and Mase, H.: Assessment of uncertainties in projecting future changes to extreme storm surge height depending on future SST and greenhouse gas concentration scenarios, *Climatic Change*, pp. 1–18, <https://doi.org/10.1007/s10584-020-02782-7>, 2020.
- Yi, S.-U.: Variations of Oceanic Condition and Mean Sea Level in the Korea Strait, pp. 125–142, 650 <https://doi.org/doi:10.1515/9780824885830-015>, 1970.
- Yoon, J. J. and Shim, J. S.: Estimation of storm surge inundation and hazard mapping for the southern coast of Korea, in: *Journal of Coastal Research*, pp. 856–861, Coastal Education Research Foundation Inc., ISSN 15515036, <https://doi.org/10.2112/si65-145.1>, 2013.
- Yoon, J. J., Shim, J. S., Park, K. S., and Lee, J. C.: Numerical experiments of storm winds, surges, and waves on the southern coast of Korea during Typhoon Sanba: the role of revising wind force, *Natural Hazards and Earth System Sciences*, 14, 3279–3295, 655 <https://doi.org/10.5194/nhess-14-3279-2014>, 2014.
- Zhang, W.-Z., Shi, F., Hong, H.-S., Shang, S.-P., and Kirby, J. T.: Tide-surge Interaction Intensified by the Taiwan Strait, *Journal of Geophysical Research: Oceans*, 115, <https://doi.org/https://doi.org/10.1029/2009JC005762>, 2010.